Département de géomatique appliquée
Faculté des lettres et sciences humaines
Université de Sherbrooke

ANALYSE DES CYCLES GEL/DÉGEL DES RÉGIONS NORDIQUES PAR TÉLÉDÉTECTION MICRO-ONDES PASSIVES EN BANDE L

Michaël Prince

Mémoire présenté pour l'obtention du grade de Maître ès sciences (M. Sc.),
cheminement recherche en télédétection

Août 2018

Identification du jury

Directeur de recherche :
Dr. Alain Royer, Professeur titulaire, Département de géomatique appliquée, Faculté des lettres et sciences humaines, Université de Sherbrooke

Co-directeur de recherche :
Dr. Alexandre Roy, Professeur, Département des Sciences de l'Environnement, Université du Québec à Trois-Rivières

Co-directeur de recherche :
Dr. Alexandre Langlois, Professeur agrégé, Département de géomatique appliquée, Faculté des lettres et sciences humaines, Université de Sherbrooke

Membres du jury :

Dr. Yannick Huot, Professeur agrégé, Département de géomatique appliquée, Faculté des lettres et sciences humaines, Université de Sherbrooke

Dr. Arnaud Mialon, Ingénieur de recherche au CNRS, CESBIO, Toulouse, France

Résumé du projet

Le réchauffement climatique dans les régions nordiques, fort important depuis le milieu du siècle dernier, a de multiples impacts sur la dynamique des écosystèmes, notamment sur les cycles gel/dégel de surface qui influencent les flux de carbone, l'activité biogéochimique des sols, l'hydrologie et le pergélisol aux hautes latitudes. La télédétection satellitaire du gel/dégel par micro-ondes passives est un outil très prometteur permettant un suivi continu et global, mais comporte des difficultés souvent reliées à l'effet d'hétérogénéité spatiale intra-pixel relié aux résolutions grossières des capteurs micro-ondes passives à basse fréquence.

L'objectif principal du projet est d'évaluer l'utilisation de la télédétection micro-onde passive en bande L (1.4 GHz) pour le suivi de l'état de gel/dégel de la surface en forêt boréale. Un premier objectif spécifique est d'évaluer un nouveau produit des cycles de gel/dégel de surface estimée à partir des radiomètres bande L satellitaires Aquarius. Cette base de données de 3.5 années a été mise en ligne au *National Snow and Ice Data Center* (NSIDC). Le deuxième objectif spécifique est d'analyser l'effet de la variabilité spatiale intrapixel de l'état de gel du sol et de son impact sur les températures de brillance (TB) mesurées par le radiomètre de la mission *Soil Moisture Active Passive* (SMAP) en période de transition afin de quantifier la fraction de sol gelé.

Les résultats pour le premier objectif montrent que la nouvelle base de données possède une bonne capacité à estimer l'état de gel/dégel de la surface sur l'ensemble de l'Hémisphère Nord (> 50°N). Cette recherche offre également une rare intercomparaison entre produits de gel/dégel satellitaires en comparant le produit Aquarius au *Freeze/Thaw-Earth System Data Record* (FT-ESDR) développé avec les données à plus hautes fréquences du capteur SSM/I. Pour le deuxième objectif, des capteurs de température distribués le long de transects de plusieurs kilomètres sur deux différents sites de taïga montrent que la variabilité spatiale du gel à l'automne peut être de 7.5 à 9.5 semaines. Il est également démontré que les mesures de SMAP sont sensibles à cette variabilité et un algorithme développé permet d'estimer le pourcentage intrapixel de sol gelé avec des coefficients de détermination (R^2) entre 0.63 et 0.88 lorsque comparé aux mesures *in situ*. Ces résultats offrent de nouveaux outils pour mieux comprendre et quantifier les cycles de gel/dégel de l'environnement boréal et leurs impacts sur les processus biogéophysiques, hydrologiques et sur le pergélisol.

Project Abstract

Climate change in nordic regions, which has been of growing significance over the past century has multiple impacts on the dynamic of ecosystems, notably on the surface freeze/thaw cycles, which influences carbon flux, soil biogeochemical activity, hydrology and permafrost at high latitudes. Satellite remote sensing of freeze/thaw with passive microwaves is a promising tool to offer continuous and global monitoring, but can also entail some difficulties due to intra-pixel spatial variability effects coming from the low resolution of low-frequency passive microwave sensors.

The primary objective of the project is to evaluate the use of passive microwave remote sensing in L-band (1.4 GHz) for monitoring of the surface freeze/thaw in the boreal forest. A first specific objective is to evaluate a new surface freeze/thaw product estimated by the Aquarius satellite L-band radiometers. This 3.5 year-old database has been put online at the National Snow and Ice Data Center (NSIDC) website. The second specific objective is to analyse the effect of intra-pixel spatial variability of freeze/thaw and its impact on brightness temperatures (TB) measured by the *Soil Moisture Active Passive* (SMAP) radiometer during transition periods in order to quantify the frozen soil fraction.

Results for the first objective show that the new database possesses a good capacity to estimate the surface freeze/thaw state for the entirety of the Northern Hemisphere (>50°N). This research also offers a rare intercomparison between freeze/thaw satellite products by comparing the Aquarius product to the *Freeze/Thaw-Earth System Data Record* (FT-ESDR) product developed with higher frequencies data of the SSM/I sensor. For the second objective, temperature sensors distributed along transects of several kilometers on two different taiga sites show that the spatial variability of autumn soil freeze onset can be between 7.5 and 9.5 weeks. It demonstrates that SMAP measurements are sensitive to this variability and a developed algorithm offers estimations of the intrapixel soil frozen fraction with coefficients of determination (R^2) between 0.63 and 0.88 when compared to *in situ* measurements.

These results offer new tools for a better understanding and quantification of freeze/thaw cycles in boreal environments and their impacts on biogeochemical and hydrologic processes and on permafrost.

Table des matières

Liste des figures

Liste des tableaux

Liste des abréviations

%fro	Frozen soil percentage in a pixel
FFrel	Frost factor index
Ffro	Fraction of frozen soil
FT	Freeze/thaw
FT-ESDR	Freeze/Thaw-Earth System Data Record
H et V	Polarisation horizontale et verticale
IGBP	International Geosphere-Biosphere Program
LCCBU	Land Cover Classifications Derived from Boston University MODIS / Terra Land Cover Data
MEaSUREs	Making Earth System Data Records for Use in Research Environnements
NASA	National Aeronautics and Space Administration
NASA/SAC-D	Aquarius de la Satellite de Aplicaciones Cientificas
NDVI	Normalized Difference Vegetation Index
NPR	Rapport de polarisations normalisé (Normalized Polarization Ratio)
NSIDC	National Snow and Ice Data Center
p	Polarisation
RMSE	Root mean square error
Rugg_Mean	Resampled ruggedness
SAT	Surface air temperature
SMAP	Soil Moisture Active Passive
SMM/I	Special Sensor Microwave Imager
SMMR	Scanning Multi-channel Microwave Radiometer
SMOS	Soil Moisture Ocean Salinity
SSMIS	SSM/I Sounder
T1 and T2	Temperature thresholds for freeze/thaw classification (article 2)
$TAVG_{day}$	Average SAT for each day
$TAVG_{week}$	Weekly resampled TAVGday
TB	Température de brillance
VWC	Vegetation water content

WMO	World Meteorological Organization
γ	Vegetation transmissivity
Γ_p	Soil reflectivity
$\Delta\varepsilon_{eau/glace}$	Contraste des permittivités électriques entre l'eau et la glace
ε	Permittivité électrique
τ	Thresholds for freeze/thaw classification (article 1)
ω_p	Effective albedo

Remerciements

Je veux tout d'abord remercier mon directeur Alain Royer et mon codirecteur Alexandre Langlois. Leurs efforts constants permettent à un grand nombre d'étudiants de vivre des expériences d'une grande richesse. Je me sens très privilégié d'avoir été membre de leur magnifique équipe.

Je tiens à honorer spécialement mon second codirecteur, Alexandre Roy, avec qui j'ai eu la chance de m'entretenir presque quotidiennement. Faire de la recherche scientifique en sa compagnie, avec rigueur et passion, mais aussi avec humour et bonne humeur, a été un équilibre parfait qui m'a soutenu pendant ces deux dernières années. La qualité retrouvée dans ce mémoire lui est en grande partie due. Je lui souhaite succès et plaisir dans sa toute nouvelle carrière en tant que professeur à l'Université du Québec à Trois-Rivières.

Je veux également remercier les professeurs qui m'ont enseigné, soit Richard Fournier, Norman T. O'Neill et Kalifa Goïta. Leur savoir et leur passion ont influencé ce projet de recherche. Grâce à eux, je peux embarquer dans le marché du travail comme géomaticien (télédect.) avec plusieurs cordes à mon arc. Un gros merci également à tous mes collègues du département qui ont rendu ces deux années riches et agréables.

Cette maîtrise a été possible grâce à la contribution financière de l'Agence Spatiale Canadienne (ASC), du Conseil de Recherches en Sciences Naturelles et en Génie du Canada (CRSNG), la Fondation Canadienne pour l'Innovation (CFI), le Centre d'étude Nordique (CEN), le Programme de Formation Scientifique dans le Nord (NSTP) et le Fond de Recherche Nature et Technologiques (FRQNT). Il faut souligner que la base de données du gel/dégel d'Aquarius a été publiée grâce au support financier de la *National Aeronautics and Space Agency* (NASA) et avec le grand soutien de Ludovic Brucker.

Finalement, je dédie cette maîtrise à ma famille, soit ma conjointe Alison Brunette pour son infini support, mes filles Joëlle et Amy pour leur source d'amour et de joie, mes parents Pierre Prince et Johanne Blouin pour le support de toute une vie.

Michaël Prince

Avant-propos

Ce mémoire est un mémoire par article. Les deux sous-objectifs sont respectivement traités dans les chapitres 2 et 3 dans deux articles. Le premier a été accepté pour publication dans Earth System Science and Data et le second, soumis à Remote Sensing of Environnement, est actuellement en révision.

Après une introduction présentant le contexte et les objectifs de recherche, ce mémoire est structuré autour de ces deux articles, contenant chacun la description des méthodologies utilisées, des résultats et des discussions. Une conclusion générale complète le document, ainsi que la liste des références bibliographiques non citées dans les articles.

1. Introduction

1.1 Contexte

La forêt boréale est le deuxième plus grand biome du globe comportant 33 % des régions forestières mondiales (FAO, 2001) et elle couvre 5.5 millions de km^2 au Canada, soit plus de la moitié du territoire canadien. Le réchauffement climatique dans cette zone boréale, important depuis le milieu du siècle dernier (Gauthier et al., 2015; Ruckstuhl et al., 2008), a de multiples impacts sur la dynamique de cet écosystème, en particulier sur les cycles de gel/dégel de surface qui influencent la saison de croissance de la végétation (Kim et al., 2014), l'activité biogéochimique des sols (Panner Selvam et al., 2016), l'hydrologie (Beer et al., 2007), le pergélisol (Schuur et al., 2015) et les flux de carbone (Kim et al, 2012 ; Richardson et al., 2010; Barr et al., 2009). Notamment, la forêt peut passer de source de CO_2 à un puits de CO_2 les années où la durée de gel est significativement réduite (Parazoo et al., 2018), car une longue saison de dégel peut engendrer une augmentation de la capacité de la végétation à capter le CO_2, alors qu'une saison plus courte va diminuer la saison de croissance et donc la captation de CO_2 par la végétation (Goulden et al., 1998). De plus, le couvert nival en zone boréale, directement lié aux conditions climatiques (précipitations et température), peut aussi jouer un rôle majeur dans cette dynamique par son effet isolant du sol (Gouttevin et al., 2012). Ainsi, mieux comprendre et suivre la variation des cycles de gel/dégel en lien avec le réchauffement climatique est un élément clé pour le suivi de la forêt boréale et sa réponse face à ces changements.

La capacité à observer globalement et quotidiennement l'état de gel/dégel du sol est limitée par la rareté des stations météorologiques, surtout dans les régions nordiques (Nalder and Wein, 1998). Même si les mesures *in situ* peuvent être interpolées en considérant la topographie et les caractéristiques des microclimats, ces méthodes ne pourraient fournir des informations suffisantes à l'échelle globale (New et al., 2000).

Les capteurs satellitaires dans les micro-ondes passives, qui dépendent de la radiation émise naturellement par la surface de la Terre, se sont avérés efficaces à détecter le gel/dégel de la surface et possèdent l'avantage d'enregistrer quotidiennement les températures de brillance (TB) à l'échelle planétaire, avec des mesures possibles autant le jour que la nuit ainsi, avec certaines

fréquences quasi insensibles aux conditions atmosphériques (Rautiainen et al., 2016; Roy et al., 2015; Kim et al., 2011). La raison est que dans les fréquences micro-ondes (entre 1 GHz et 50 GHz), la permittivité électrique (ε), qui influence l'émissivité du rayonnement électromagnétique (Demontoux et al., 2008), possède un fort contraste entre l'état gelé et dégelé de l'eau ($\Delta\varepsilon_{eau/glace}$; Artemov and Volkov, 2014; Figure 1). La résultante est que la TB subira une augmentation marquée lors de la transition de phase de l'eau vers la glace et une diminution semblable pour le passage inverse.

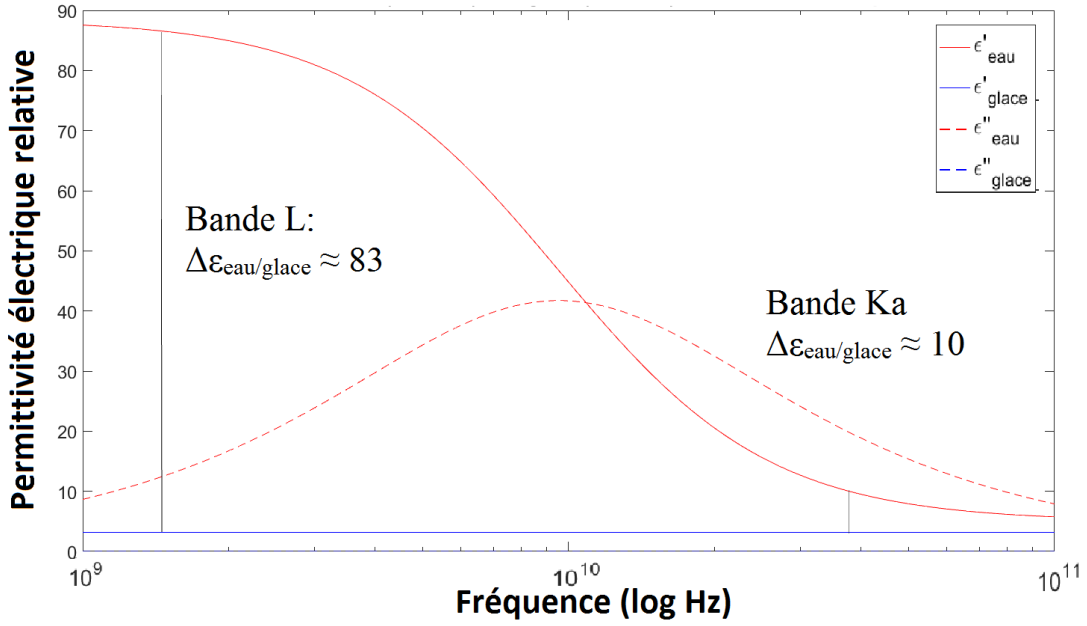

Figure 1 : Permittivité électrique de l'eau (T= 273 K) et de la glace (T=273 K) en fonction de la fréquence. ε' est la partie réelle et ε'' est la partie imaginaire. ε''est nulle pour la glace aux fréquences de 1 à 100 GHz.

1.2 Problématique

Il existe le produit *Freeze/Thaw Earth System Data Record* (FT-ESDR), un produit satellitaire de gel/dégel faisant partie du projet *Making Earth System Data Records for Use in Research Environnements* (MEaSUREs) de la *National Aeronautics and Space Administration* (NASA). Le produit offre des données du gel/dégel sur l'ensemble du globe pour une période continue s'étendant de 1979 jusqu'à 2016 (Kim et al., 2011; 2017). Il a été développé grâce à la série de capteurs *Scanning Multi-channel Microwave Radiometer* (SMMR), *Special Sensor Microwave Imager* (SMM/I) et SSM/I Sounder (SSMIS). L'algorithme du FT-ESDR permet de cartographier

dans une résolution spatiale de 25 km quatre états : gelé toute la journée, dégelé toute la journée, en transition (gelé le matin et dégelé l'après-midi), en transition inverse (dégelé le matin et gelé l'après-midi). Toutefois, les références *in situ* qui ont permis d'évaluer le produit se limitent strictement à la température de l'air (Kim et al., 2017). Quoiqu'il s'agisse d'une bonne indication du processus physique de l'état de l'environnement (Roy et al., 2015), étant donné l'interaction entre l'atmosphère et les surfaces, l'état du sol demeure incertain. De plus, l'algorithme du FT-ESDR se base uniquement sur la TB à 37 GHz en polarisation verticale, correspondant à une longueur d'onde d'environ 0,8 cm. La radiation à ces plus courtes longueurs d'onde peut fortement entrer en interaction avec l'ensemble des différents éléments se retrouvant dans un pixel (Ulaby et al., 1986). Il y a donc une grande incertitude à savoir exactement ce à quoi le signal gel/dégel est relié, et plus concrètement, à quel niveau le sol, la neige, la structure et la phénologie de la végétation contribuent au signal. De plus, à cette fréquence, le contraste des permittivités entre l'eau et la glace est plus faible.

Depuis les dernières années, une série de missions ont rendu possible l'observation satellitaire en bande L (1.4 GHz), telles que les missions *Aquarius* de la *Satellite de Aplicaciones Cientificas* (NASA/SAC-D; 2011-2015; Le Vine et al., 2010), *Soil Moisture Ocean Salinity* (SMOS) de la *European Space Agency* (ESA; 2010-présent; Kerr et al., 2010) et dernièrement *Soil Moisture Active Passive* de la NASA (SMAP; 2015-présent; Entakhabi et al., 2010). Avec une longueur d'onde d'environ 21 cm, la radiation captée dans cette bande devrait être moins sujette à interagir avec la végétation (Ulaby et al., 1986) et la neige sèche (Picard et al., 2013), puisque les branches et le feuillage des arbres et la taille des grains de neige sont beaucoup plus petits que la longueur d'onde. Il a été démontré que le rapport des TB en polarisation horizontale et verticale (H et V) diminue drastiquement à l'automne à cause de la chute de la constante diélectrique relié au gel du sol, demeure bas durant l'hiver et augmente significativement durant le printemps lorsque la constante diélectrique reprend des valeurs caractéristiques de sol dégelé (Derksen et al., 2017; Brucker et al., 2014; Rautiainen et al., 2012). D'autres études ont relié l'émission dans la bande L avec la profondeur de gel dans le sol (Rautiainen et al., 2014) et la température (Mironov et al., 2013). En somme, la télédétection en basse fréquence micro-ondes peut fournir de l'information différente et complémentaire sur le gel/dégel par rapport à celles fournies par des fréquences plus élevées, entre autres en étant plus sensible au contraste diélectrique relié aux gel/dégel du sol.

Dans ce sens, une étude approfondie des capteurs Aquarius et SMOS fut réalisée afin de vérifier la capacité à détecter le gel/dégel du sol en bande L par satellite (Roy et al., 2015). Cette recherche a entre autres estimé l'état de gel/dégel de surface en se basant sur le rapport de polarisations normalisé [NPR = $(TB_V - TB_H) / (TB_V + TB_H)$] qui est un indice sensible à l'état de gel/dégel (Rautiainen et al., 2014). Les résultats montrent que le NPR dans les régions de toundra change drastiquement lors des transitions intersaisonnières de gel/dégel de surface (Figure 2), avec des valeurs de NPR stables lors des périodes de gel hivernales et de dégel estivales. Par contre, dans les régions en forêt boréale, les transitions intersaisonnières sont moins distinctes, résultant à un taux de précision plus faible de la détection du gel/dégel lorsque les mesures satellitaires sont comparées aux valeurs in situ. Davantage de recherches doivent donc se réaliser pour déterminer l'effet du continuum sol/végétation sur la TB durant les périodes de gel/dégel en forêt boréale.

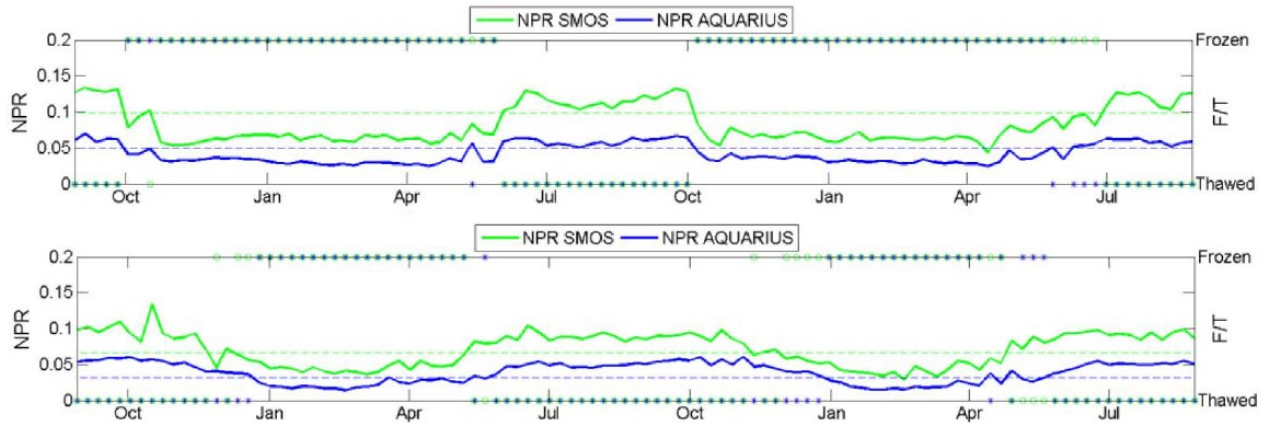

Figure 2: Série temporelle (2011-2013) du NPR avec estimation de l'état de gel/dégel (FT) dérivé de SMOS et d'Aquarius en zone de toundra (en haut) et en zone de forêt boréale (en bas) (inspiré de Roy et al., 2015).

De plus, de récentes études (Roy et al., 2017a; Lemmetyinen et al., 2016; Schwank et al., 2015, 2014) ont démontré que la neige « sèche » (sans présence d'eau liquide) a un certain impact sur la TB en bande L émise par le sol. La neige augmente la TB, allant dans le même sens que le signal engendré par un sol gelé. À l'opposé, la présence d'eau dans la neige absorbe la radiation et réduit la TB perçue par les radiomètres satellitaires, produisant un effet comparable à un dégel du sol (Roy et al., 2017a). Le couvert nival demeure donc une difficulté supplémentaire à surmonter

dans le but de comprendre le lien entre le signal en bande L et les conditions de gel/dégel des surfaces.

Actuellement, les produits satellitaires de gel/dégel classifient qualitativement l'état de surface, avec une approche à un seuil pour délimiter les deux classes (Kim et al., 2017; Derksen et al., 2017; Roy et al., 2015). Toutefois, les transitions de phase de l'environnement ne se réalisent pas abruptement et une coexistence des états se manifeste, particulièrement sur l'ensemble d'un territoire compris dans une empreinte de radiomètre satellitaire (entre 12 km et 40 km). Dans la méthode en conception du produit SMOS (Rautiainen et al., 2016), une classe « partiellement gelé » a été créée pour tenir compte de ce phénomène. Du côté de SMAP, une étude récente fait dans les prairies Canadiennes laisse entrevoir la possibilité que le radiomètre satellitaire soit sensible à la proportion de sols gelés à l'intérieur de ses pixels de 36 km de résolution (Rowlandon et al., 2018). En comparant le NPR dérivé des mesures de SMAP à des mesures in situ de gel/dégel sur plusieurs sites intrapixel durant quelques journées, le NPR a effectivement réagi proportionnellement à la quantité de surface gelée. De plus amples recherches doivent être menées pour valider la possibilité d'estimer une fraction de sol gelé dans un pixel à partir de la mesure satellitaire.

À ce jour, le seul produit offrant une estimation quotidienne sur le gel/dégel conçu en bande L sur l'ensemble du globe est celui de SMAP, alors que le nouveau produit Aquarius offre une information hebdomadaire. À noter qu'un produit SMOS (Rautiainen et al., 2016) est en développement, mais il n'est présentement pas disponible. De plus, à notre connaissance, aucun produit satellitaire en bande L n'a été comparé au FT-ESDR, qui est en bande Ka, pour observer des différences notables entre leurs estimations. Pourtant, il est connu que la bande L est la plus sensible à l'humidité du sol et qu'elle est moins affectée par la rugosité de la surface, la vapeur d'eau et la végétation (Kerr, 1996). À l'opposé, l'émission en bande Ka a une plus forte sensibilité à l'eau liquide des nuages, à la rugosité et à la végétation, mais elle est moins sensible à l'humidité du sol. Puisque la différence de permittivité électrique entre l'eau et la glace est plus grande en bande L ($\Delta\varepsilon_{eau/glace} \approx 83$) qu'en bande Ka ($\Delta\varepsilon_{eau/glace} \approx 10$) (Artemov and Volkov, 2014), la bande L devrait avoir un signal plus contrasté lors des transitions de phase dans le sol. Étant donné la relation entre la fréquence et le comportement physique du rayonnement micro-

onde, une comparaison entre produits de gel/dégel à différentes fréquences est nécessaire à la compréhension de l'information que procurent ces différents produits.

Finalement, il est crucial de mentionner que la principale difficulté de la télédétection satellitaire passive en micro-ondes est la résolution spatiale grossière des produits de TB, qui se situe généralement entre 25 et 36 km (Derksen et al., 2017; Rautiainen et al., 2016; Brucker et al., 2014; Kim et al., 2011). L'effet de l'hétérogénéité de l'environnement comprise dans une telle superficie demeure une source d'incertitude et un défi à relever pour la communauté scientifique. Des campagnes de mesures sur le terrain et aéroportées ont mis en évidence la difficulté de relier la mesure de TB satellitaire à l'information sur l'ensemble du territoire sous le pixel (Roy et al., 2017b; Langlois et al., 2011; Derksen et al., 2005). La densité et le type de végétation, la présence d'étendues d'eau, la topographie, les caractéristiques du couvert nival (hauteur, densité, taille des grains), l'humidité, la rugosité et la composition du sol sont des facteurs influençant l'émission de micro-ondes. Ces paramètres peuvent varier au mètre près (Rutter et al., 2014), ne permettant pas de relier aisément une donnée in situ relativement ponctuelle à son pixel associé de la mesure satellitaire. À notre connaissance, il y a très peu d'études qui ont analysé l'impact de la variabilité spatiale des différentes composantes de l'environnement sur l'estimation de l'état de gel/dégel du sol en forêt boréale à l'échelle des pixels micro-onde passifs satellitaires.

1.2 Objectifs

L'objectif principal du projet est d'évaluer l'utilisation de la télédétection micro-onde passive en bande L (1.4 GHz) pour le suivi de l'état de gel/dégel de la surface en forêt boréale. Cette recherche est, entre autres, une contribution pour aider la caractérisation de la dynamique annuelle du cycle du carbone terrestre en lien avec la durée de gel du sol et la phénologie des écosystèmes boréaux. Deux objectifs spécifiques distincts, mais complémentaires permettent de répondre à l'objectif principal du projet.

Le premier objectif spécifique est d'évaluer un nouveau produit gel/dégel de surface estimé par les radiomètres satellitaires en bande L d'Aquarius que nous avons développé et mis disponible en ligne au National Snow and Ice Data Center (NSIDC) (Roy et al., 2018), ainsi que de le comparer au produit du *Freeze/Thaw-Earth System Data Record* (FT-ESDR) développé à partir des TB à 37 GHz.

Le deuxième objectif spécifique est d'analyser l'effet de la variabilité spatiale intrapixel de l'état de gel du sol à l'automne et de son impact sur la variation temporelle des signaux TB de SMAP en période de transition pour développer un nouvel algorithme permettant de quantifier la fraction de sol gelé.

Chacun de ces objectifs spécifiques fait l'objet d'un article scientifique. Le premier (section 2) est a été accepté pour publication et le second (section 3) est présentement en révision.

1.3 Hypothèses

L'hypothèse associée au premier objectif spécifique est :

- Qu'il existe des différences entre les produits de gel/dégel d'Aquarius et du FT-ESDR puisqu'ils sont conçus à partir de fréquences micro-ondes différentes et que ces différences peuvent mener à des informations complémentaires sur l'état de la surface.

Les hypothèses associées au deuxième objectif spécifique sont :

- Que l'étude des températures de sol *in situ* distribuées spatialement va améliorer notre compréhension de l'effet de variabilité spatiale de l'état de gel/dégel du sol sur la TB mesurée en bande L en forêt boréale.
- Que les TB mesurées par le radiomètre satellitaire de SMAP sont sensibles à la fraction de surface de sol gelé à l'intérieur d'un même pixel en forêt boréale permettant ainsi le développement d'un algorithme estimant la fraction de sol gelé.

2. Produit gel/dégel de surface en Bande L sur l'hémisphère nord conçu à partir des radiomètres satellitaires d'Aquarius

« Northern Hemisphere Surface Freeze/Thaw Product from Aquarius L-band Radiometers »

Michael Prince[1,2], Alexandre Roy[3,2,1], Ludovic Brucker[4,5], Alain Royer[1,2], Youngwook Kim[6], Tianjie Zhao[7]

[1] Centre d'Applications et de Recherches en Télédétection (CARTEL), Université de Sherbrooke, Sherbrooke, QC J1K 2R1, Canada
[2] Centre d'Étude Nordique, Québec, Canada
[3] Département des Sciences de l'Environnement, Université du Québec à Trois-Rivières, Trois-Rivières, QC, Canada, G9A5H7
[4] NASA Goddard Space Flight Center, Cryospheric Sciences Laboratory, Code 615, Greenbelt, MD 20771, USA
[5] Universities Space Research Association, Goddard Earth Sciences Technology and Research Studies and investigations, Columbia, MD 21044, USA
[6] Numerical Terradynamic Simulation Group, College of Forestry & Conservation, The University of Montana, Missoula, MT 59812, USA
[7] State Key Laboratory of Remote Sensing Science, Institute of Remote Sensing and Digital Earth, Chinese Academy of Sciences, Beijing, China

Article publié au *Earth System Science Data* (ESSD).

Référence:

Prince, M., Roy, A., Brucker, L., Royer, A., Kim, Y., and Zhao, T.: Northern Hemisphere surface freeze–thaw product from Aquarius L-band radiometers, Earth Syst. Sci. Data, 10, 2055-2067, https://doi.org/10.5194/essd-10-2055-2018, 2018.

2.1 Présentation de l'article

Cette étude évalue le nouveau produit de gel/dégel de surface conçu à partir des radiomètres d'Aquarius (FT-AP) selon l'algorithme développé par Roy (2015). Le produit est disponible sur le site de la NSIDC (https://nsidc.org/data/aq3_ft/versions/5). L'évaluation du produit s'est faite par une intercomparaison avec le produit FT-ESDR, sur la période de chevauchement des produits (2011-2014) sur l'ensemble de l'hémisphère nord au-dessus du parallèle 50°N. Cette analyse à grande échelle offre une intercomparaison entre produits issus de différentes bandes (L et Ka), permettant ainsi de mettre en évidence les ressemblances et les divergences qui pourraient provenir de la variation du comportement des micro-ondes selon les fréquences. De plus, cette analyse possède l'avantage de considérer la forêt boréale dans son entièreté, contenant également les régions de l'Eurasie, en plus de couvrir des régions de toundra et de milieux ouverts.

Pour cet article, ma contribution a consisté à l'analyse par intercomparaison des bases de données, à l'écriture et à la publication de l'article. De plus, j'ai contribué à la publication de la base de données FT-AP sur le site du NSIDC. Plus précisément, Alexandre Roy a initialement codé le programme pour faire rouler sur l'ensemble de l'hémisphère nord. J'ai validé la bonne qualité du produit et j'ai vérifé qu'il a été aplliqué convenablement. Puis, Ludovic Brucker a finalisé la base de données pour sa publication au NSIDC.

2.2 Article 1

Abstract. In the Northern Hemisphere, seasonal changes in surface freeze/thaw (FT) cycles are an important component of surface energy, hydrological and eco-biogeochemical processes that must be accurately monitored. This paper presents the weekly polar-gridded Aquarius passive L-Band surface freeze/thaw product (FT-AP) distributed on the Equal-Area Scalable Earth Grid version 2.0, above the parallel 50° N, with a spatial resolution of 36 km x 36 km. The FT-AP classification algorithm is based on a seasonal threshold approach using the normalized polarization ratio, references for frozen and thawed conditions and optimized thresholds. To evaluate the uncertainties of the product, we compared it with another satellite FT product also derived from passive microwave observations but at higher frequency: the resampled 37 GHz FT Earth Science Data Record (FT-ESDR). The assessment was carried out during the overlapping period between 2011 and 2014. Results show that 77.1% of their common grid cells have an agreement better than 80%. Their differences vary with land cover type (tundra, forest and open land) and freezing and thawing periods. The best agreement is obtained during the thawing transition and over forest areas, with differences between product mean freeze or thaw onsets of under 0.4 weeks. Over tundra, FT-AP tends to detect freeze onset 2–5 weeks earlier than FT-ESDR, likely due to FT sensitivity to the different frequencies used. Analysis with mean surface air temperature time series from six in situ meteorological stations shows that the main discrepancies between FT-AP and FT-ESDR are related to false frozen retrievals in summer for some regions with FT-AP. The Aquarius product is distributed by the U.S. National Snow and Ice Data Center (NSIDC) at https://nsidc.org/data/aq3_ft/versions/5 with the doi:10.5067/OV4R18NL3BQR.

1 Introduction

Seasonal freezing and thawing affect over half of the Northern Hemisphere. Landscape freeze/thaw (FT) state transitions show highly variable spatial and temporal patterns, with measurable influences to climate (IPCC, 2014; Peng et al., 2016; Poutou et al., 2004), hydrological (Gouttevin et al., 2012; Gray et al., 1985), ecological (Kumar et al., 2013; Black et al., 2000) and biogeochemical processes (Panneer Selvann et al., 2016; Xu et al., 2013; Schaefer et al., 2011). The surface FT state affects the latent heat exchange and the energy balance at the

interface between soil surface and the overlying medium. The vegetation growing season is sensitive to the annual non-frozen period (Kim et al., 2012), while vegetation net primary production and net ecosystem CO_2 exchange with the atmosphere is impacted by FT timing variability (Barr et al., 2009; Kurganova et al., 2007). Comprehensive in situ observational long-term datasets for soil state characteristics across terrestrial environments are still limited or inadequate, mostly for northern remote regions. Remote sensing in the thermal emission domain offers great potential for detecting changes in land-surface temperature, but is strongly limited by clouds, vegetation and snow cover (e.g. Langer et al., 2013). Spatially and temporally continuous information on soil freeze/thaw changes is lacking for the regions of both seasonal frozen ground and permafrost.

Passive microwave remote sensing has proven sensitive to the surface FT state due to large changes in surface dielectric properties between predominantly frozen and non-frozen conditions, and it offers global coverage. The remotely sensed FT detection capability at L-band (1.4 GHz) has been developed and validated in several studies (Zheng et al., 2017; Roy et al., 2017b; Rautiainen et al., 2012; Schwank et al., 2004). In the L-band, the shallow depth contributing to the radiation (around 5 cm for an unfrozen soil) and the strong permittivity difference between water and ice ($\Delta\varepsilon_{ice/water}$) make it favourable for FT retrieval (Rautiainen et al., 2012; 2014). In recent years, passive L-band FT algorithms were created for NASA's Aquarius (Roy et al., 2015), ESA's soil moisture and ocean salinity (SMOS) (Rautiainen et al., 2016), and NASA's soil moisture active/passive (SMAP) (Derksen et al., 2017) missions. An FT Earth Science Data Record (FT-ESDR) was also produced using a higher microwave frequency at Ka-band (37 GHz) (Kim et al., 2017a). This product offers consistent and continuous global daily information on the FT state for several decades (1979-2016; Kim et al., 2017b). Observations were recorded by the scanning multi-channel microwave radiometer (SMMR), the special sensor microwave/imager (SSM/I), and the SSM/I Sounder (SSMIS).

This study presents the new Aquarius passive FT product for the Northern Hemisphere (Roy et al., 2018), distributed by the US National Snow and Ice Data Center (NSIDC) at https://nsidc.org/data/aq3_ft/versions/5. The product precision and uncertainties are addressed by comparing Aquarius FT retrievals with the FT-ESDR product for the overlapping period (2011 - 2014). The Aquarius passive FT product (referred to as FT-AP hereinafter) is based on the

Aquarius weekly Level-3 L-Band brightness temperature (TB) product (Brucker et al., 2015; NSIDC: http://nsidc.org/data/AQ3_TB/versions/5). The algorithm uses a relative frost factor (FFrel; see e.g. Rautiainen et al., 2014) based on normalized polarization ratio (NPR) temporal change detection (Roy et al., 2015). To our knowledge, few intercomparisons between L- and Ka-band FT products exist (Derksen et al., 2017), and none evaluated inter-annual variability differences. However, it is well established that different frequencies interact differently with ground components (vegetation, soil, snow), canopy, etc. For instance, observations at L-band are less sensitive than at Ka-band to snow, plant biomass and surface roughness (Ulaby et al., 1986). Being less prone to disturbances above the ground, the L-band emission should give better information on the ground state in forested and snow-covered areas. In addition, since $\Delta\varepsilon_{ice/water}$ is larger at L-band ($\Delta\varepsilon_{ice/water} \approx 83$) than at Ka-band ($\Delta\varepsilon_{ice/water} \approx 10$) (Artemov and Volkov, 2014), there should be a higher sensitivity to the ground phase transition at L-band. Hence, because differences between products can be attributed to the microwave frequency and the algorithm used, the FT-AP is also compared with surface air temperature (SAT) observations.

The main objective of this study is to present and evaluate the weekly FT-AP by comparing it to the FT-ESDR and to SAT observations across the Northern Hemisphere. First, we describe the new FT-AP product, designed by the algorithm developed by Roy et al. (2015), but applied across the Northern hemisphere. Then, we investigate the spatial and temporal FT variations from both FT-AP and FT-ESDR products over the Northern hemisphere. We then investigate the cause of the main differences between products from in situ information. The comparison aims to identify the similarities and differences between L-band and Ka-Band FT products for further improvements of FT monitoring across the Northern hemisphere.

2. Method

2.1 Aquarius passive FT product (FT-AP)

The Aquarius FT product was generated using the Aquarius weekly averaged polar gridded L-band TB product distributed on the EASE-Grid 2.0, above the parallel 50° N, with a spatial resolution of 36 km x 36 km (Brucker et al., 2014). This formatted TB was specially designed for the study of northern regions. For each Aquarius radiometers, the product averages TB values

calculated from every measurement made during a week, combining ascending and descending orbits. The FT classification algorithm is based on a seasonal threshold approach (STA) using frost factor index (FFrel) (Eq. 1), introduced by Rautiainen et al. (2014), where FF_{NPR} is the frost factor based on the normalized polarization ratio between TB at vertical and horizontal polarizations (TB_V and TB_H; Eq. 2). FF_{fr} and FF_{th} are reference frozen and thawed frost factors obtained for each pixel and each radiometer by averaging, respectively, the five minimum FF_{NPR} found during winters (January and February) and five maximum FF_{NPR} found during summers (July and August) over the three available dataset period.

$$FFrel = \frac{FF_{NPR} - FF_{fr}}{FF_{th} - FF_{fr}} \quad (1)$$

$$FF_{NPR=} = \frac{TB_V - TB_H}{TB_V + TB_H} \quad (2)$$

A threshold (τ) was determined by optimization to classify the surface as frozen or thawed if the FFrel is lower or higher than the threshold (Eq. 3).

$$\begin{aligned} &\text{If} \quad FFrel < \tau \rightarrow \text{freeze} \\ &\text{or if} \quad FFrel > \tau \rightarrow \text{thaw} \end{aligned} \quad (3)$$

The thresholds optimized (Table 1) in Roy et al. (2015) over Northern America for three basic land covers (tundra, forest, open land) were applied over the Northern Hemisphere using the Land Cover Classifications derived from Boston University MODIS / Terra Land Cover Data (LCC_{BU}) (see Sect. 2.4). The optimization method calculates the threshold that gives the best accuracy when the product retrievals is compared to in situ air temperature stations. It was shown that optimized thresholds only slightly improved the accuracies by 1% to 4% compared to a fixed threshold of 0.5. For tundra site, a broad range of threshold values ([0.3-0.7]) caused an insignificant variation of accuracy.

Table 1: Thresholds (τ) applied in Eq. 3 for the whole circumpolar area, derived from the Roy et al. (2015)

Beam	Tundra	Forest	Open land
1	0,41	0,46	0,31
2	0,69	0,55	0,31
3	0,63	0,54	0,41

Aquarius operated three non-scanning radiometers at different incidence angles (29.2°, 38.4° and 46.3°) and with different 3 dB footprint sizes (respectively 76 km x 94 km, 84 km x 120 km and 97 km x 156 km). Based on the LCC_{BU}, the thresholds found in Roy et al., (2015) were used to create FT maps for each radiometer. The three FT maps were then blended to create a fourth map, which offers more complete spatial coverage. For every grid cell, radiometer 2 (38.4°) was prioritized, then radiometer 1 (29.2°) was used, while radiometer 3 was only used if data from the other radiometers were not available for the given grid cell. This blended algorithm was chosen based on the performance given for each radiometer in Roy et al. (2015) (radiometer 2 gave the best results, while radiometer 3 gave the worst results). Due to the width of Aquarius' swath and its revisit time, 16.5% of the terrestrial 36-km grid cells have less than 95% observations over the period and 16% were not measured at all. Thus, the intercomparison with the FT-ESDR product (Sect. 2.2) was only made when FT-AP data were available for a given date. The time span for this analysis runs from August 2011 with the first Aquarius observations to 31 December 2014 with the latest FT-ESDR data available at the time of our analysis.

2.2 FT-ESDR product

The first version of the FT-ESDR product (Kim et al., 2011) was based on an STA similar to the FFrel but applied exclusively to the TB_V at 37 GHz instead of the NPR. In the new extended product (Kim et al., 2017b; NSIDC: https://nsidc.org/data/nsidc-0477/versions/4), a modified seasonal threshold algorithm (MSTA) was used to determine thresholds for each grid cell to obtain better accuracy. It consists of a grid-cell-wise weighted empirical linear regression relationship between the 37 GHz TB_V measurements and daily surface air temperature estimates from the ERA-Interim global reanalysis.

The extended FT-ESDR product used in this study is derived from the SSM/I 37 GHz brightness temperatures (footprint of 38 km x 30 km) and resampled at a grid cell resolution of 25 km on the global Ease-Grid v1.0. The observations were recorded twice per day, which gives the possibility of attributing discrete frozen or thawed states for morning and afternoon. The final classification offers four discrete surface states: "frozen all day", "thawed all day", "frozen in AM and thawed in PM" (transitional) and "thawed in AM and frozen in PM" (inverse-transitional). In this study, the latter two classes were combined into a single transitional class. In order to compare the two

products, the FT-ESDR was first spatially resampled to the EASE-Grid 2.0 with the nearest neighbor method choosing the smallest distance between pixel centers. Then, FT-ESDR was temporally resampled at the same weekly calendar than the FT-AP. The temporal FT-ESDR sampling procedure was based on the rule that the most frequently occurring class over the seven days of a week is adopted as the value for the entire week. In cases where the frozen and thawed classes occurred with equal frequency during a single week (e.g. two days frozen, two days thawed and three days transitional), the transitional class was attributed. This latter class occurs mainly during the transition seasons of spring and fall. Thus, we assigned the transitional class to thawed class during spring and summer since it indicates the beginning of the thawing process and we assigned the transitional class to the frozen class during fall and winter since it indicates the beginning of the freezing process. This FT-ESDR resampling procedure ensured that the two products were at the same temporal and spatial resolutions with only the frozen and thawed categories, making comparison possible.

2.3 Land cover classification

The land cover information (Fig. 1) comes from the EASE-Grid 2.0 LCC_{BU} (Brodzik *and* Knowles, 2011; NSIDC: nsidc.org/data/nsidc-0610/versions/1), using the same grid as the FT-AP product. The seventeen land cover classes were grouped to obtain four classes: tundra, forest, open land (savanna, cropland and grassland) and water (see Roy et al., 2015). Each grid cell was assigned its single most prominent class of land cover which is used for the selection its thresholds (Table 1). All grid cells with more than 20% of water and ice indicated by the LCC_{BU} were masked.

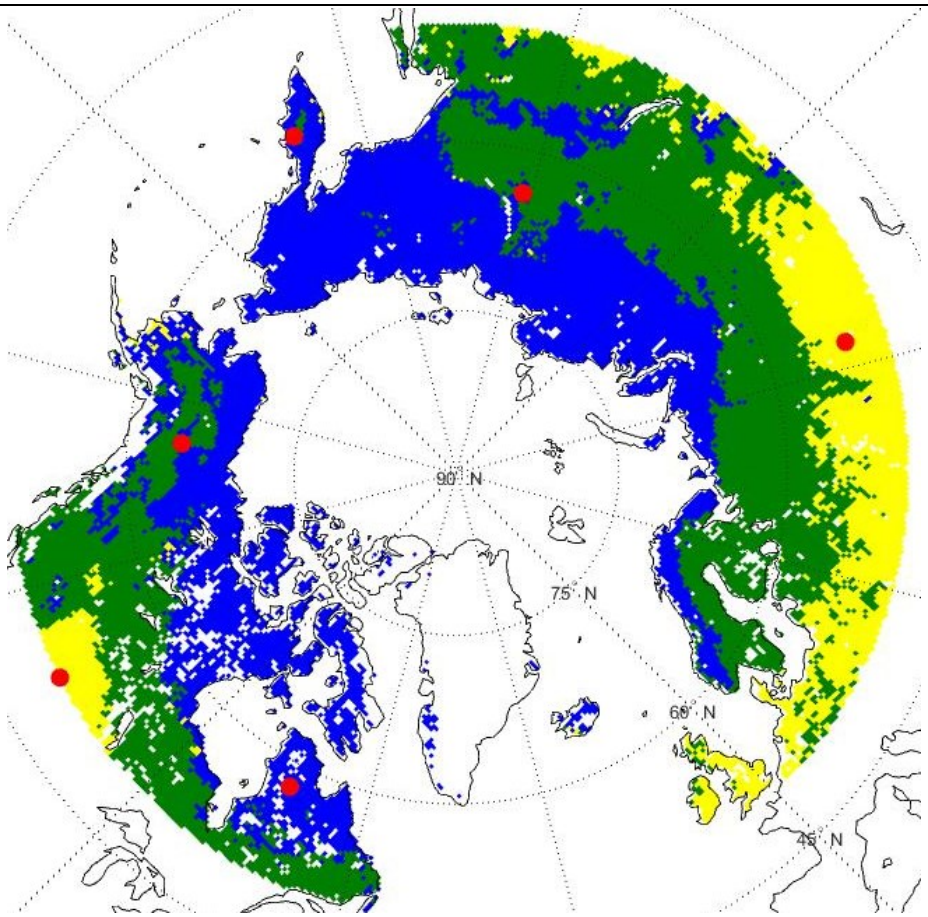

Figure 1: Land cover classes: tundra (blue), forest (green), open land (yellow) and water/ice mask (white). Red dots show weather station locations

2.4 Weather stations

Six weather stations (Table 2) were selected for validation from the National Climatic Data Center (NCDC) Climate Data Online website (CDO, https://www.ncdc.noaa.gov/cdo-web/datasets). Two tundra, two forest and two open land sites were chosen for a comparison between the product classifications and the in situ SAT. All of the sites are more than 200 km from a coast, except the Kamchatka site; its distance of about 85 km from the sea may have an influence on the large L-band field of view. The average SAT for each day ($TAVG_{day}$) were used to create a time series for each site. For statistical purposes, the weekly resampling method used on the FT-ESDR product was also applied to the SAT daily values, using 0°C as the threshold between frozen and thawed states ($TAVG_{week}$) (see Roy and al., 2015).

Ruggedness values from a 30 arc-second resolution elevation map (Gruber 2012; University of Zurich: http://www.geo.uzh.ch/microsite/cryodata/pf_global/) were resampled to the EASE-Grid 2.0 with the drop in the bucket approach. In order to represent a ruggedness value at the Aquarius footprint scale, the mean value of a 3 x 3 grid cell window centered on each weather station pixel was calculated (Rug_Mean). To each value was attributed a class according to the Gruber (2012) classification.

Table 2: Latitude, longitude and land cover of each weather station (See also Fig.1)

Country/Region	Land Cover	Lat. (N)	Long.	Ruggedness	Rug_Mean
Kamchatka/Kljuchi	Tundra	56.3167	160.8331	Undulating	Hilly
Canada/Québec	Tundra	57.9167	-72.9833	Undulating	Undulating
US/Alaska	Forest	64.7761	-141.162	Mountainous	Mountainous
Russia/Siberia	Forest	63.7831	121.6166	Flat	Flat
Kazakhstan	Open land	53.2166	63.6166	Flat	Flat
Canada/Saskatchewan	Open land	50.2666	-107.733	Undulating	Undulating

3 Results

3.1 Spatial FT analysis

Figure 2a shows the percentage of concordant classifications between the two products for the 3.7 year overlapping period. Overall, the results show that there is good agreement between the two products. In general, forest areas have a better percentage of concordance than other land covers. However, some regions show important discrepancies, especially along coastal margins and in mountainous and open areas (such as in northern Europe, Kazakhstan (and surroundings) and the Canadian Prairies). Those lower percentages correspond to regions where lower accuracies to detect the FT were already noted in Roy et al. (2015) and Kim et al. (2017a) (see Sect. 4). Figure 2b shows that 77.1% of the common grid cells have more than 80% agreement. More specifically, 41.6% of the grid cells have more than 90% agreement over 3.7 years, with 10.0% of them having more than 95%. About 35.5% of the grid cells have an agreement between 80% and 90%; only 22.8% of the cells have an agreement lower than 80%.

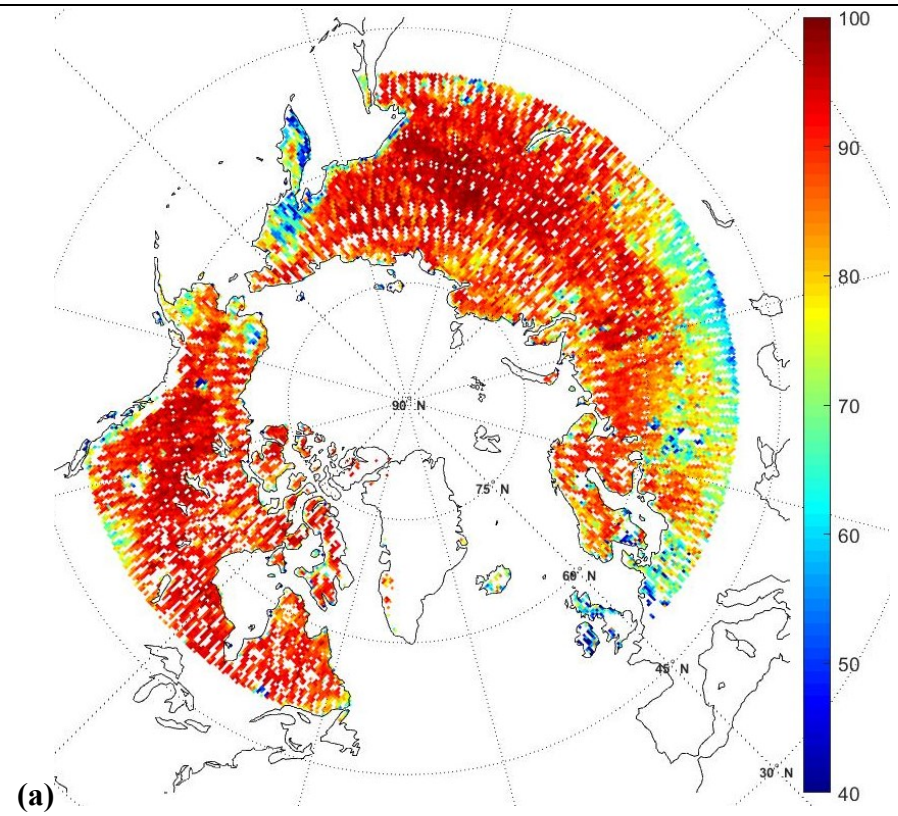

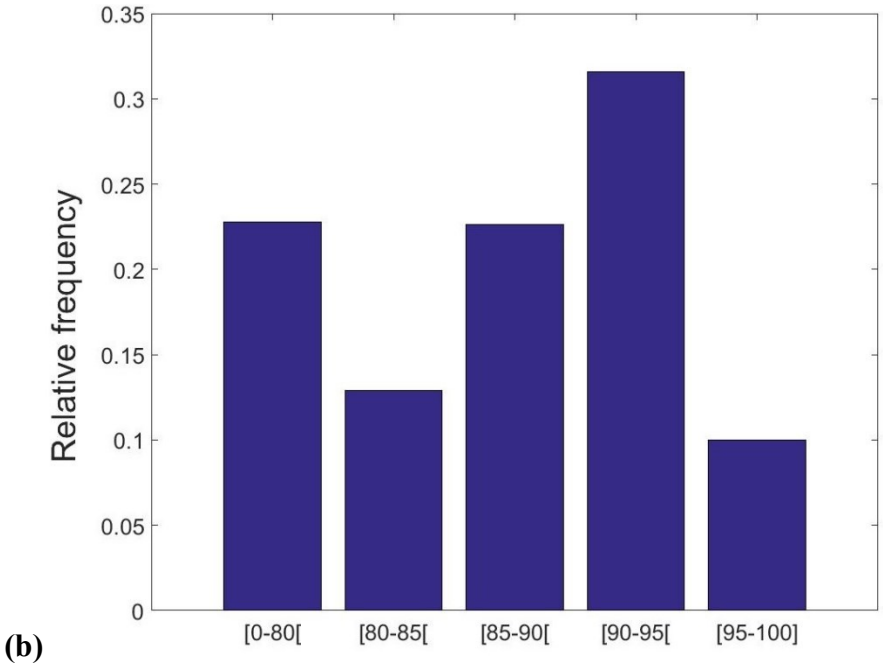

Figure 2: (a) Map of the percentage agreement between FT-AP and FT-ESDR classification for the whole period studied and (b) derived frequency distribution of the mean percentage agreement over the whole study area (Lat. > 50° N).

3.2 Temporal analysis

An analysis was made to identify similarities and differences between the two products used for retrieving surface FT state during the freezing (fall) and thawing (spring) periods. For each land cover type, Figure 3 shows the time series of the fraction of land frozen (for all land at latitudes greater than 50° N). To reduce the effect of obvious false frozen retrievals in summer (discussed below) on the analysis and to focus on the differences primarily related to the physics of the measurements (i.e., L-band vs. Ka-band), only grid cells with an agreement percentage between FT-AP and FT-ESDR higher than 80% (from Fig. 2a) were considered. Light blue zones indicate periods for which the FT-ESDR transitional class is set to the frozen class (see Sect. 2.2).

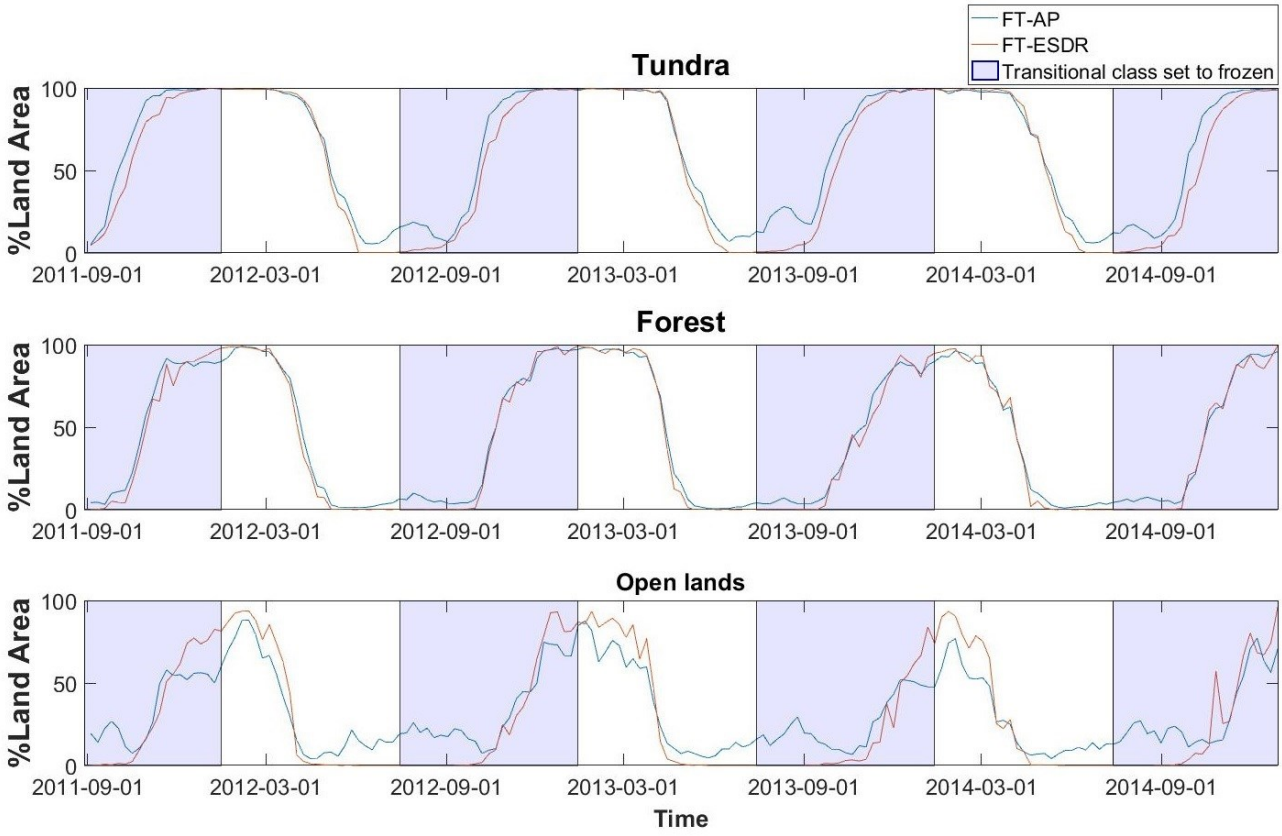

Figure 3: Time series of percentage of frozen grid cells for FT-AP and FT-ESDR for the three land covers (tundra, forest and open lands).

Figure 3 gives information on temporal differences between the products. The difference between FT-AP and FT-ESDR in terms of the percentage of frozen grid cells for a given day (Δ%frozen) is greatest during falls in tundra, at 10–27%. In forest, Δ%frozen is much lower than in tundra,

with differences of 0–12%. For these two land covers (tundra and forest), the agreement between the products varies by year. In fall, the horizontal shift between the curves indicates time delays (Δtime) for the two products to reach the same percentage of frozen grid cells. In tundra, Δtime ranges from 1–3 weeks. In forest, Δtime is always less than one week. This result demonstrates an excellent overall consistency between the products. However, FT-AP shows the percentage of frozen land increasing every summer to a peak that is not perceived with FT-ESDR. In tundra, those maximum values vary between 17% (2014) and 28% (2013) and are lower in forest at 7% (2013) and 10% (2012). Even if some of those detections represent the real state of the surface, the FT-AP peaks may be mainly caused by false frozen detections, which were noticed in the SMAP product (Derksen et al., 2017). False frozen detections are identified in our analysis using observations from the weather stations (Fig. 6, Sect. 3.3). In open land, FT-AP retrievals tend to vary frequently by showing noticeable unexpected frozen retrievals in summer and thawed retrievals in winter (blue lines in Fig. 3). FT-ESDR shows almost no frozen regions in summer, but unfrozen regions in winter, evidence that the open land regions are at the southern limits of the freeze regions. This in turn makes retrieval more difficult due to the higher temporal variability in FT events in winter.

To spatially represent the information provided by Δtime, maps in Fig. 4 indicate the week of the year of the freeze onset for each product (top and middle maps). The freeze onset is defined as the first week of the year when the state changed from thawed to frozen and stayed frozen for two more consecutive weeks. This variable can only be identified for grid cells that contain observations over several weeks in a row and have good agreement (>80%) according to Fig. 2a. Figure 4 also shows the difference in freeze onset between the two products (bottom maps), defined as FT-AP minus FT-ESDR. A negative value means that FT-AP detects the freeze onset earlier than FT-ESDR (represented by cold colors) and inversely for a positive value (represented by warm colors).

Comparing FT-AP and FT-ESDR maps shows a global tendency of FT-AP to reach the freeze onset 2–5 weeks earlier than FT-ESDR in the tundra regions (blue zones in Fig. 4). In 2013 and 2014 (Fig. 4c–d), this tendency is stronger, with more regions experiencing an earlier freeze onset by 3–5 weeks according to FT-AP. While these differences are less noticeable in the forest, some local discrepancies are observable with noticeable inter-annual variabilities.

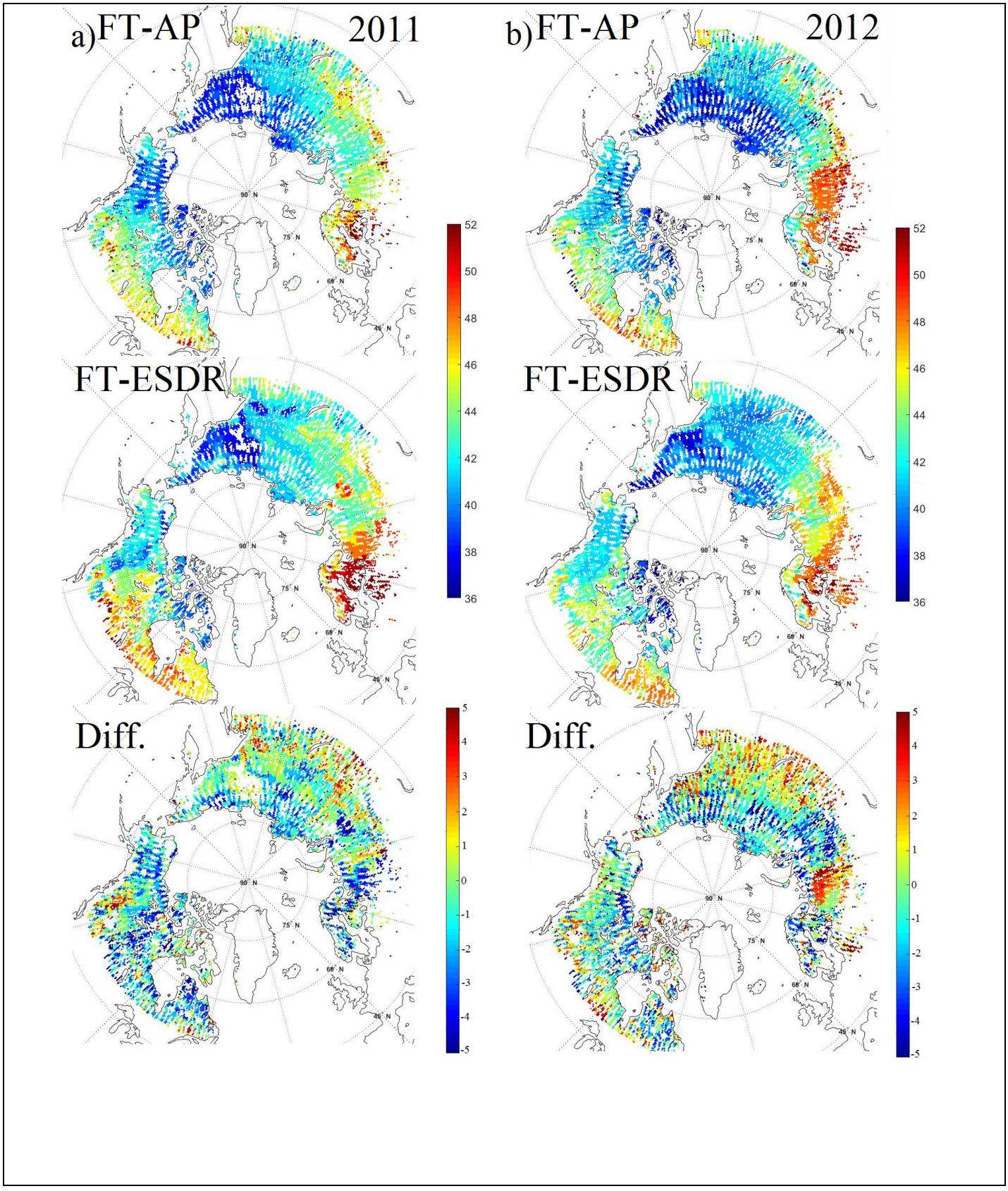
a) FT-AP 2011
b) FT-AP 2012
FT-ESDR
FT-ESDR
Diff.
Diff.
90° N
75° N
60° N
45° N
52
50
48
46
44
42
40
38
36
5
4
3
2
1
0
-1
-2
-3
-4
-5

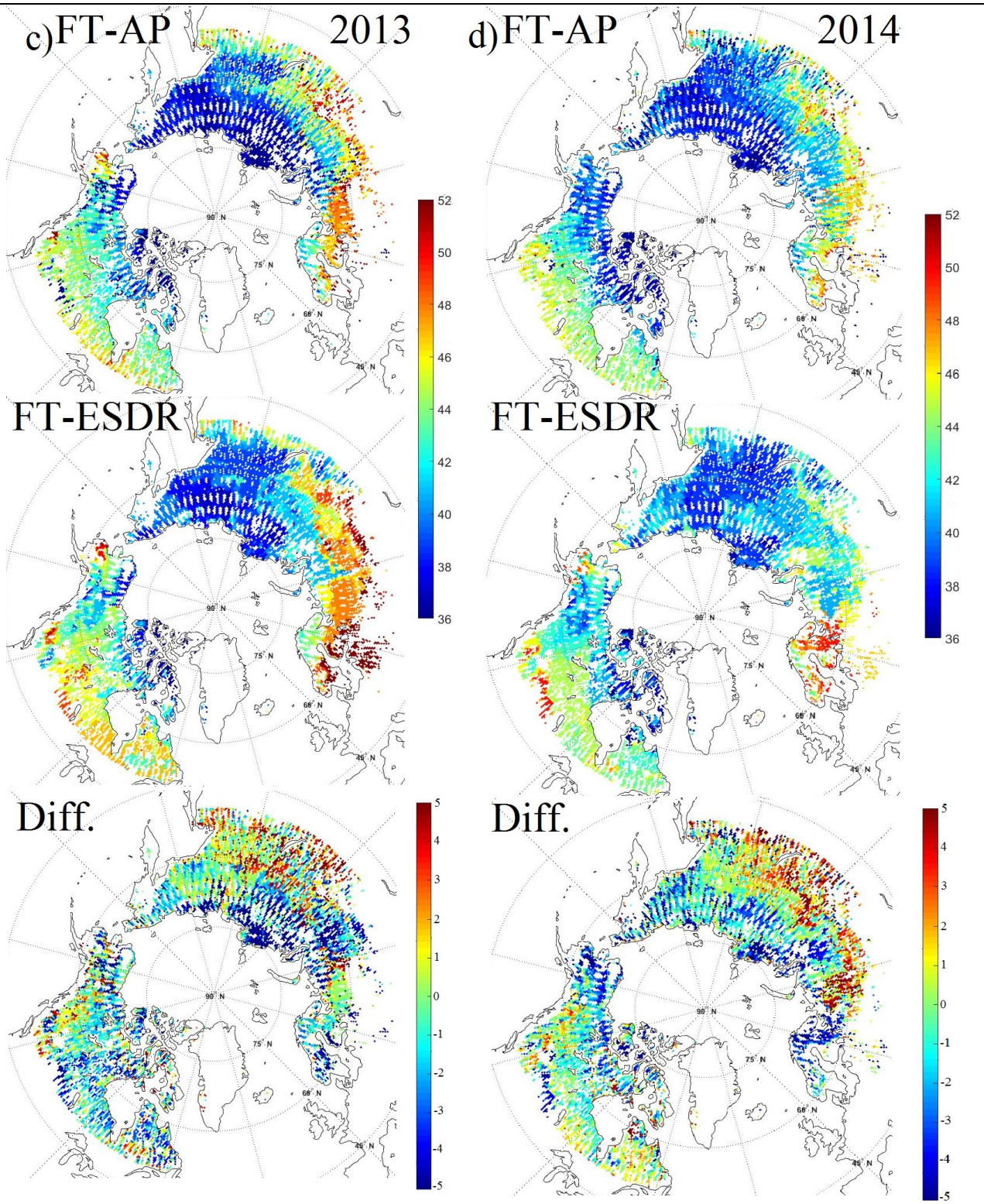

Figure 4: Freeze onset maps, where colors indicate the week of year, for a) 2011, b) 2012, c) 2013 and d) 2014 with FT-AP (top), FT-ESDR (middle) and difference between the products (Diff. = FT-AP minus FT-ESDR; bottom)

Table 3 gives freeze onset means (μ) and standard deviations (σ) in weeks of the year for each land cover and year. Over tundra, it shows the greatest freeze onset mean difference ($\Delta\mu = \mu_{FT\text{-}AP}$ minus $\mu_{FT\text{-}ESDR}$) between the two products in 2013, with $\Delta\mu$ = 2.4 weeks, and the smallest difference in 2011, with $\Delta\mu$ = 1.3 weeks. Over forest, the differences are much smaller; the greatest occurs in 2011, with $\Delta\mu$ = 0.7 weeks, and the smallest in 2012, with $\Delta\mu$ = 0.0 weeks. As noted for Fig. 4, FT-AP tends to detect freeze onset earlier than FT-ESDR. These freeze onset differences suggest that there is a divergence in the FT signal at L and Ka bands, and that there might be complementary information in the two signals (this is further addressed in the discussion).

Table 3: Mean (μ), standard deviation (σ) and mean difference (Δμ) between products of freeze onset date (week of the year) for each land cover

		2011		**2012**		**2013**		**2014**		**All years**
		μ	**σ**	**μ**	**σ**	**μ**	**σ**	**μ**	**σ**	**μ**
Tundra	**FT-AP**	40.6	2.5	39.7	3.5	38	4.7	38.6	3.5	39.2
	FT-ESDR	41.9	2.9	41.1	2.9	40.4	3.2	40.6	2.6	41
	Δμ	**-1.3**		**-1.4**		**-2.4**		**-2**		**-1.8**
Forest	**FT-AP**	43.8	2.9	43.5	3.6	43.5	3.7	42.4	3.3	43.3
	FT-ESDR	44.5	3.2	43.5	3.0	44.2	3.8	42.3	2.9	43.6
	Δμ	**-0.7**		**0**		**-0.7**		**0.1**		**0.3**
Open lands	**FT-AP**	45.8	2.8	46	4.8	45.2	4.7	44.9	3.6	45.5
	FT-ESDR	47.1	3.4	45.7	3.0	48.6	3.7	44.6	3.2	46.5
	Δμ	**-1.3**		**0.3**		**-3.4**		**0.3**		**-1**

For the thawing period, differences between the products according to Fig. 3 and Table 4 are small for all land covers, meaning that globally the two products respond similarly to landscape thaw. This result is consistent across land covers and for the three spring seasons available for this analysis with a stronger variability for open lands. The sensitivity of passive microwave frequencies to the water present in the snow at the beginning of the thaw explains the similarity between the products in spring (Roy et al., 2017a; Hallikainen et al., 1986). Thaw onset maps created from the difference of thaw onset between the products (bottom maps), defined as FT-AP minus FT-ESDR, illustrate the consistency between products, but highlight some local differences (Fig. 5).

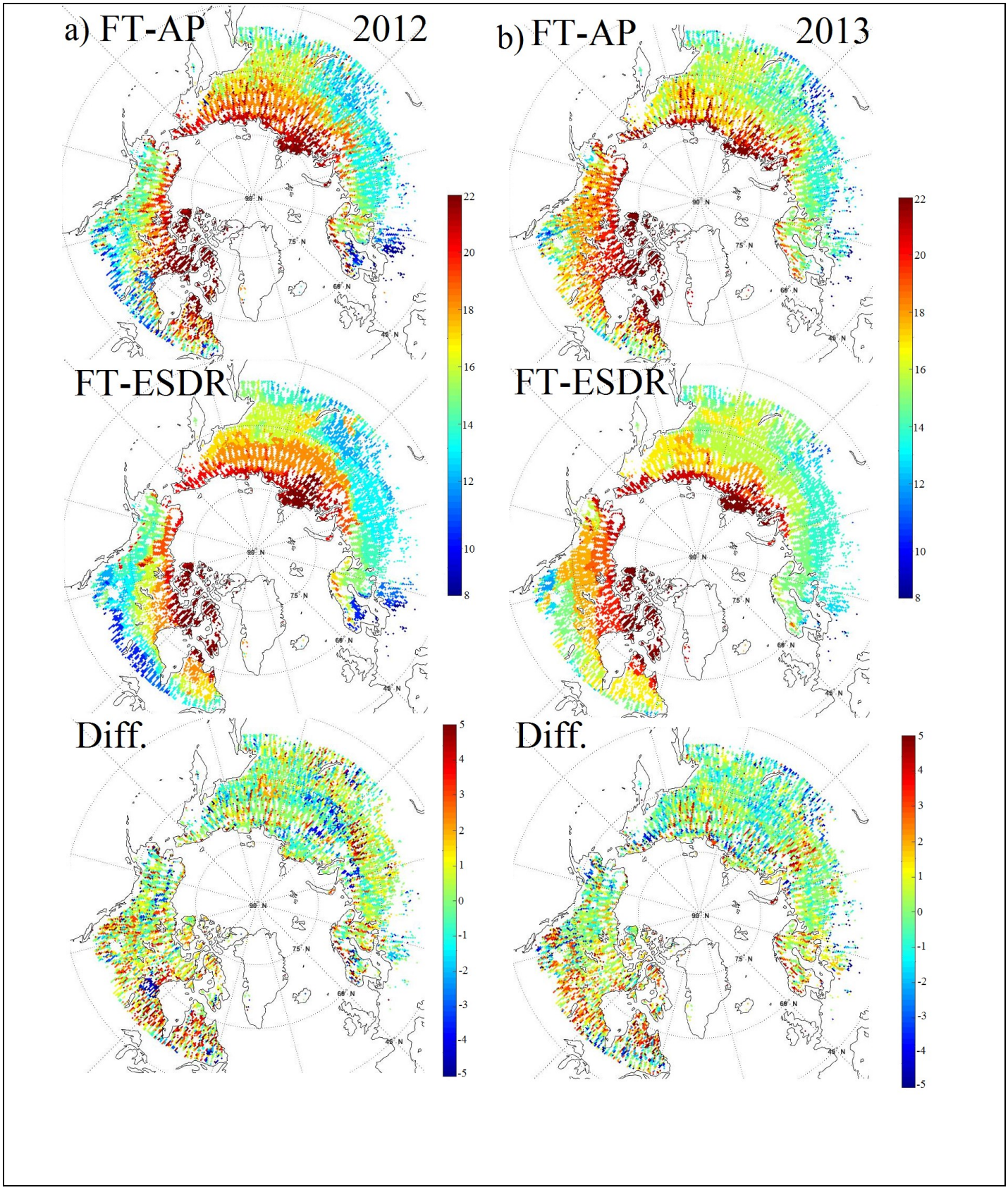
a) FT-AP 2012
b) FT-AP 2013
FT-ESDR
FT-ESDR
Diff.
Diff.
90° N
75° N
60° N
45° N
22
20
18
16
14
12
10
8
5
4
3
2
1
0
-1
-2
-3
-4
-5

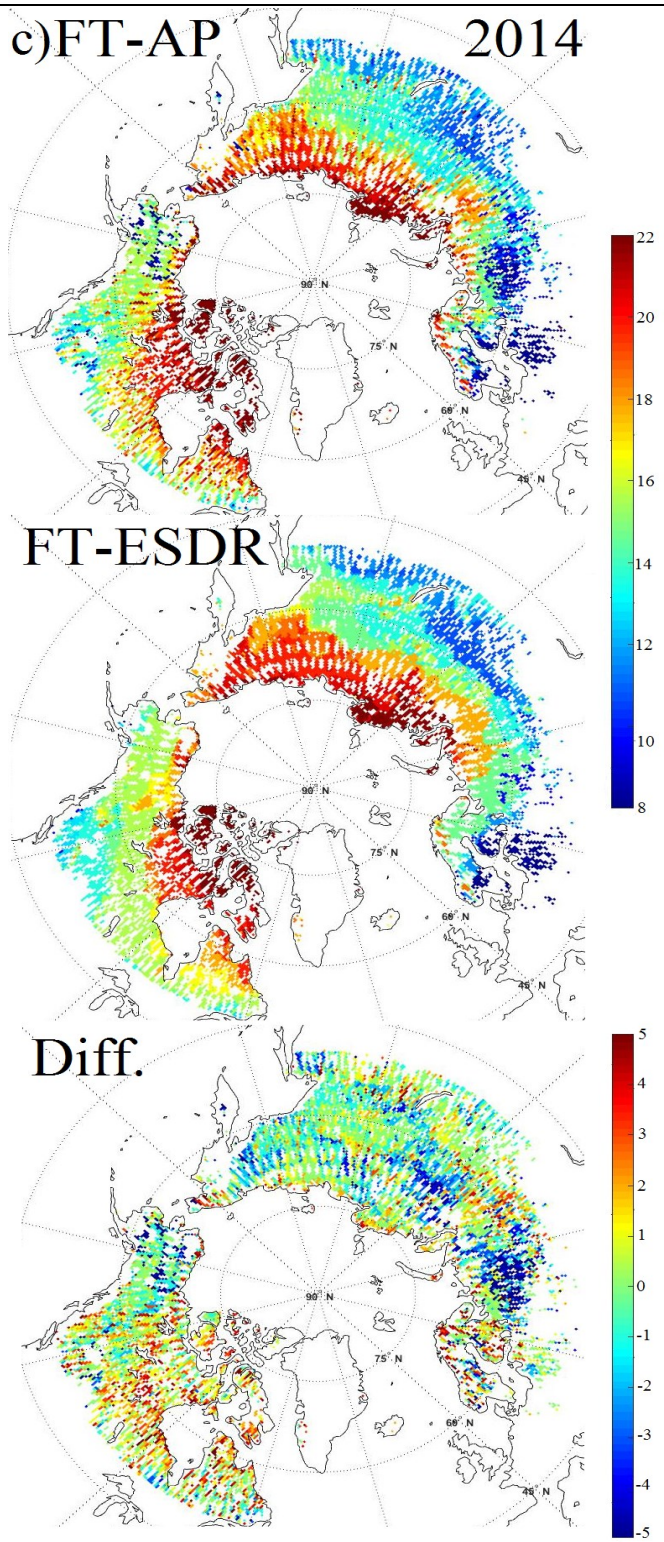

Figure 5: Thaw onset maps, where colors indicate the week of year, for a) 2012, b) 2013 and c) 2013 with FT-AP (top), FT-ESDR (middle) and difference between the products (Diff. = FT-AP minus FT-ESDR; bottom)

Table 4: Means (μ), standard deviation (σ) and means difference between products of thaw onset date (week of the year) for each land cover

		2011		2012		2013		All years
		μ	**σ**	**μ**	**σ**	**μ**	**σ**	**μ**
Tundra	**FT-AP**	19.1	3	19.1	3.2	18.8	3.6	19.0
	FT-ESDR	18.7	2.3	18.7	2.4	18.8	2.5	18.7
	Δμ	**0.4**		**0.4**		**0**		**0.3**
Forest	**FT-AP**	14.7	2.3	15.4	2	13.7	3	14.6
	FT-ESDR	14.3	2	15.3	1.5	14	2.4	14.5
	Δμ	**0.4**		**0.1**		**-0.3**		**0.1**
Open lands	**FT-AP**	11.9	2.4	13.3	3	11.2	3.5	12.1
	FT-ESDR	12.1	1.9	14	1.7	11.6	2.9	12.6
	Δμ	**-0.2**		**-0.7**		**-0.4**		**-0.4**

3.3 Comparison with weather stations

In Sect. 3.1, it was shown that there were some regions where both products show significant discrepancies. In order to better assess the observed variabilities, we looked at six different sites (Fig. 1) to evaluate the temporal evolution of both FT products and compared them to SAT measurements. The objective was to identify any difficulties the products may have monitoring FT in particular conditions. SAT was chosen as in situ reference since Roy et al. 2015 showed that SAT was the best proxy to validate satellite FT products. Table 5 shows the percentages of agreement of weekly FT detection over the entire period between FT-AP, FT-ESDR and $TAVG_{week}$ (Fig.6a-f). The mean agreement between the satellite products and in situ measurement is 81.6% for FT-AP and 92.0% for FT-ESDR. Discontinuities in the series (Fig.6a-f) is caused by the absence of Aquarius observations in a given week.

Table 5: Agreement (%) of weekly FT detections between FT-AP and FT-ESDR and between satellite products and in situ data ($TAVG_{week}$) for each site over the entire period. The sites are defined in Table 2.

Country/Region	Land Cover	FT-AP / FT-ESDR (%)	FT-AP / $TAVG_{week}$ (%)	FT-ESDR / $TAVG_{week}$ (%)
Kamchatka/Kljuchi	Tundra	68.7	67.9	94.3
Canada/Québec	Tundra	83.8	90.8	89.7
US/Alaska	Forest	87.7	88.9	94.3
Russia/Siberia	Forest	97.1	97.7	97.1
Kazakhstan	Open lands	66.3	70.9	92.0
Canada/Saskatchewan	Open lands	76.2	73.3	84.6
Mean		80.0	81.6	92.0

At the Kamchatka site (Fig. 6a, Table 5), FT-AP has a low agreement with $TAVG_{week}$ at 67.9%. The error occurs mostly in summers with obvious false frozen misclassifications, since SAT is over 0°C during that period. In contrast, there is a strong agreement of 94.3% between FT-ESDR and $TAVG_{week}$, with differences occurring in the transitional period with no specific pattern between the years. The difficulty in the retrieval could be due to the fact that the Kamchatka site's grid cell has a very low difference between the minimum and maximum NPR values (Δ_{NPR}) used to create FF_{fr} and FF_{th}, with Δ_{NPR} = 0.015 and Δ_{NPR} = 0.021 for radiometers 2 and 3, respectively. This low difference may lead to a lower sensitivity to FT. Moreover, there is change of ruggedness classification (Table 2) from the one grid cell ruggedness (SSM/I footprint scale) to the Rug_M (Aquarius footprint scale) from undulating to mountainous. With a coastline at about 85 km, a major difference of spatial variability exists between SSM/I and Aquarius measurements over the Kamchatka site.

The Quebec site (Fig. 6b), also over tundra land cover, has better product agreements with $TAVG_{week}$ than the Kamchatka site, with percentages around 90%. FT-AP has generally a better agreement with $TAVG_{week}$ during the fall freezing periods. There are only minor exceptions due to a few false frozen retrievals in summer. These exceptions show a typical situation in which FT-AP detects the freeze onset earlier than FT-ESDR, as mentioned in Sect. 3.2. The relatively high Δ_{NPR} (Δ_{NPR} = 0.024 and 0.032 for radiometers 1 and 2, respectively) could be a factor generating fewer false flag retrievals than in the Kamchatka site grid cell.

For forest sites (Fig. 6c–d), both products have good agreement with $TAVG_{week}$. The statistics for the Siberia site highlight the highest agreement: 97.7% for FT-AP and 97.1% for FT-ESDR. Interestingly, the forest sites have Δ_{NPR} values comparable to those of the tundra sites, with Δ_{NPR} = 0.022 and 0.029 for radiometers 2 and 3 respectively in Siberia, and a unique Δ_{NPR} = 0.010 for radiometer 1 in Alaska. The latter value is the lowest of all the sites in this study. Since Alaska has relatively good FT-AP agreements (87.7% with $TAVG_{week}$ and 88.9% with FT-ESDR), clearly small differences between FF_{fr} and FF_{th} alone cannot explain the false frozen retrieval problem at L-band.

At the open land sites, the low agreement (Fig. 6e–f) between FT-AP and $TAVG_{week}$ (70.9% in Kazakhstan and 73.3% in Saskatchewan) is mainly due to the false frozen retrieval in summer. During the transitional period, the FT-AP is in good agreement with $TAVG_{week}$, sometimes better than FT-ESDR, especially in the fall of 2012, 2013 and 2014 in Kazakhstan. Nevertheless, FT-ESDR agrees relatively well, with 92.0% in Kazakhstan and 84.6% in Saskatchewan. The winter of 2011 in Saskatchewan was particularly warm, and the products reacted differently to a succession of over 0°C events, which affected the overall agreement percentage. The Δ_{NPR} of the open land sites are 0.088 for radiometer 2 in Kazakhstan and 0.029 and 0.095 for radiometers 1 and 3 in Saskatchewan. Consequently, since these are the highest values of all sites, in this case, the false frozen retrievals cannot be explained by a small value of Δ_{NPR}.

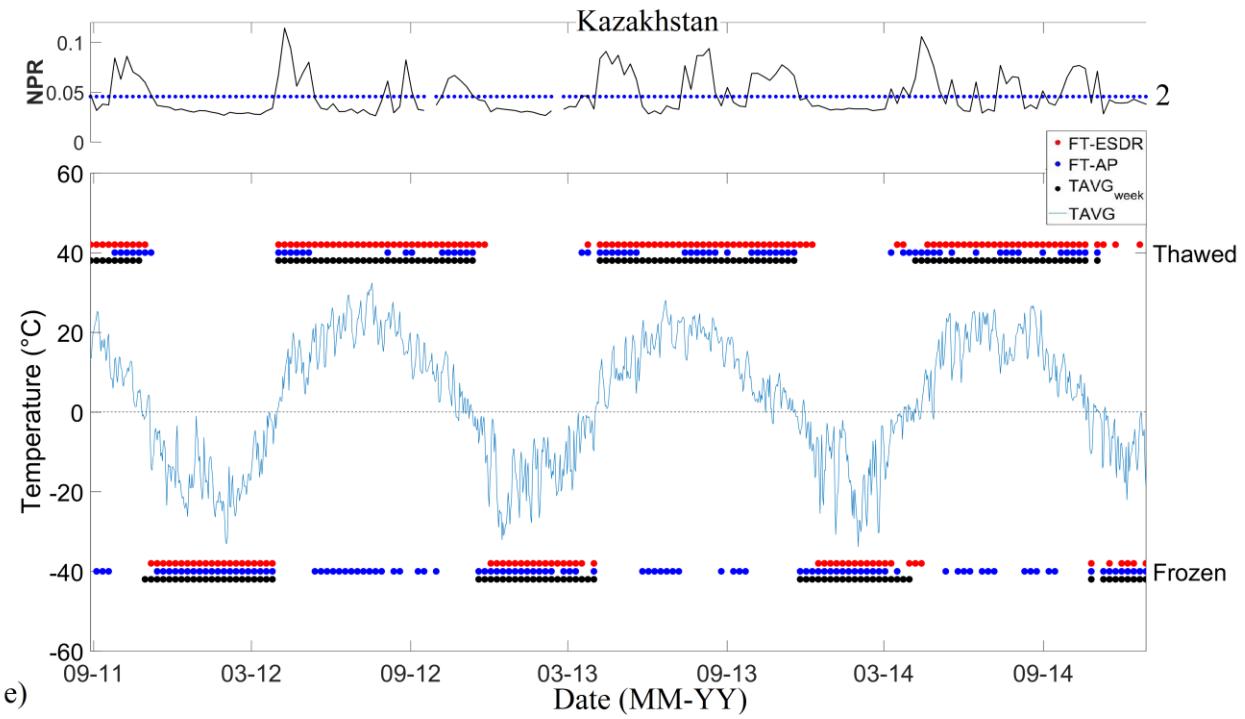
Kazakhstan
NPR
0.1
0.05
0
2
FT-ESDR
FT-AP
TAVG_week
TAVG
60
40
20
0
-20
-40
-60
Thawed
Frozen
Temperature (°C)
09-11
03-12
09-12
03-13
09-13
03-14
09-14
Date (MM-YY)

e)

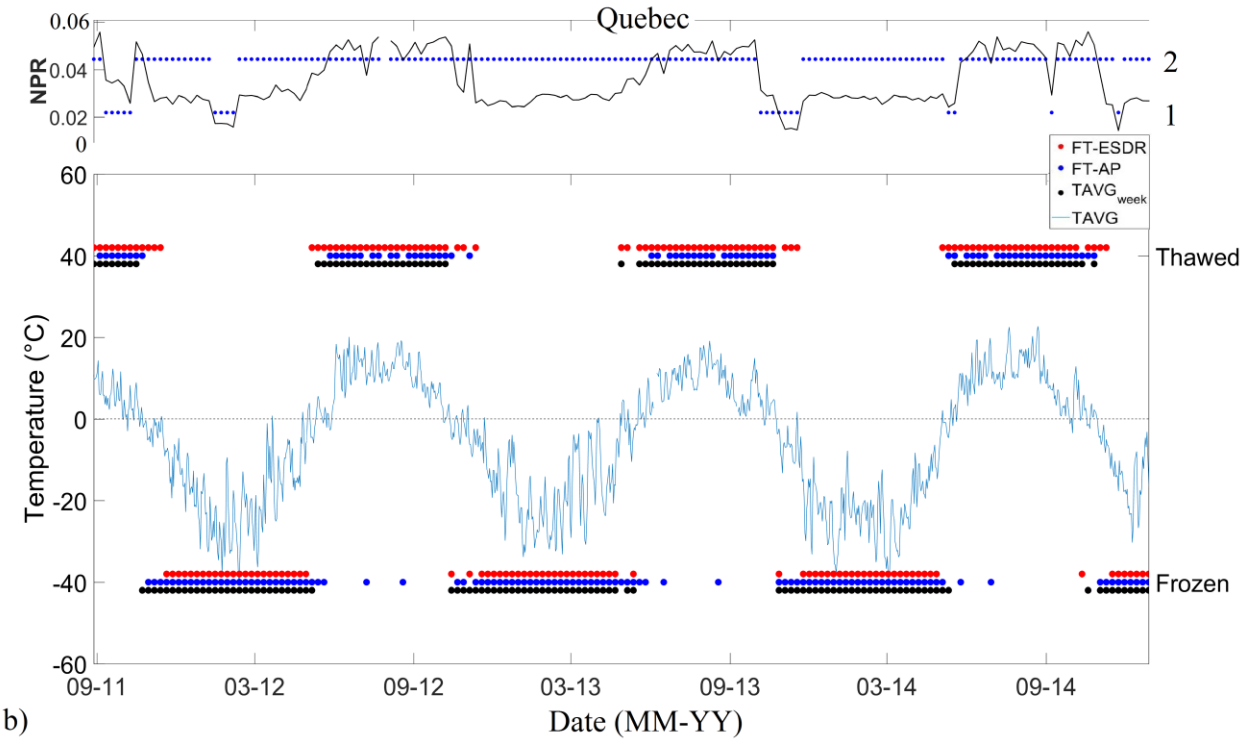
Quebec
NPR
0.06
0.04
0.02
0
2
1
FT-ESDR
FT-AP
TAVG_week
TAVG
60
40
20
0
-20
-40
-60
Thawed
Frozen
Temperature (°C)
09-11
03-12
09-12
03-13
09-13
03-14
09-14
Date (MM-YY)

b)

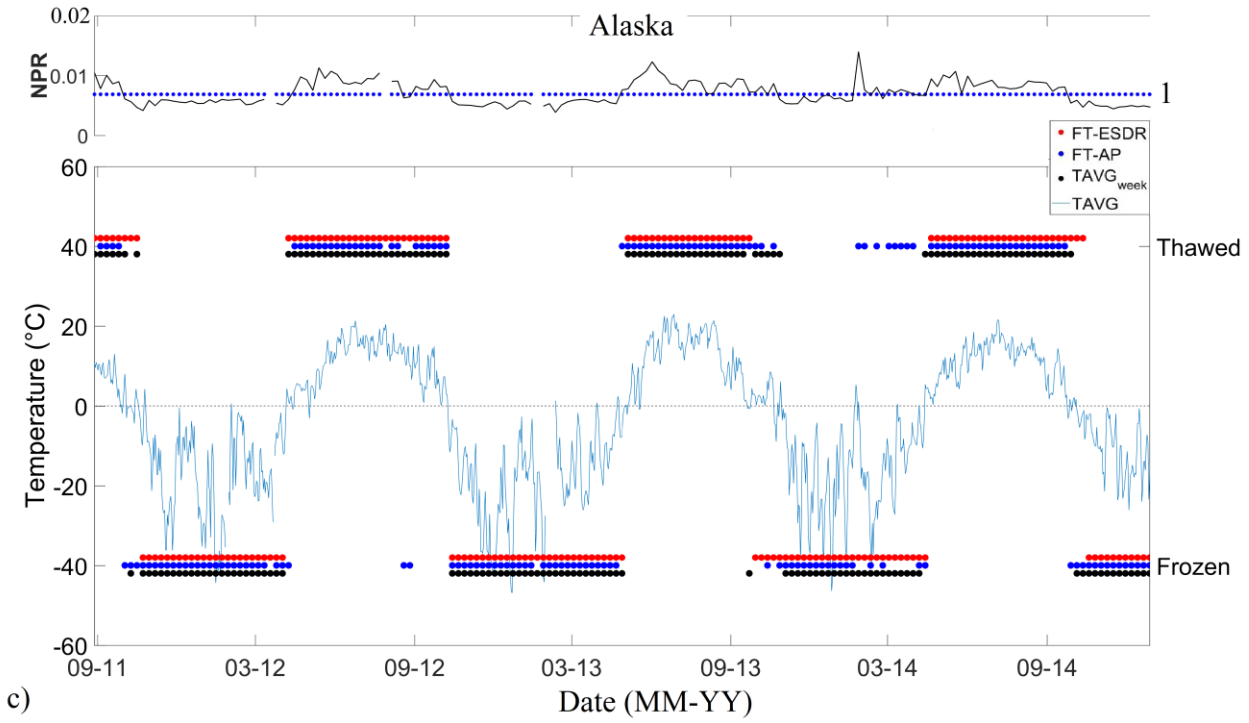
Alaska
NPR
0.02
0.01
0
1
FT-ESDR
FT-AP
TAVG week
TAVG
60
40
20
0
-20
-40
-60
Thawed
Frozen
Temperature (°C)
09-11
03-12
09-12
03-13
09-13
03-14
09-14
Date (MM-YY)

c)

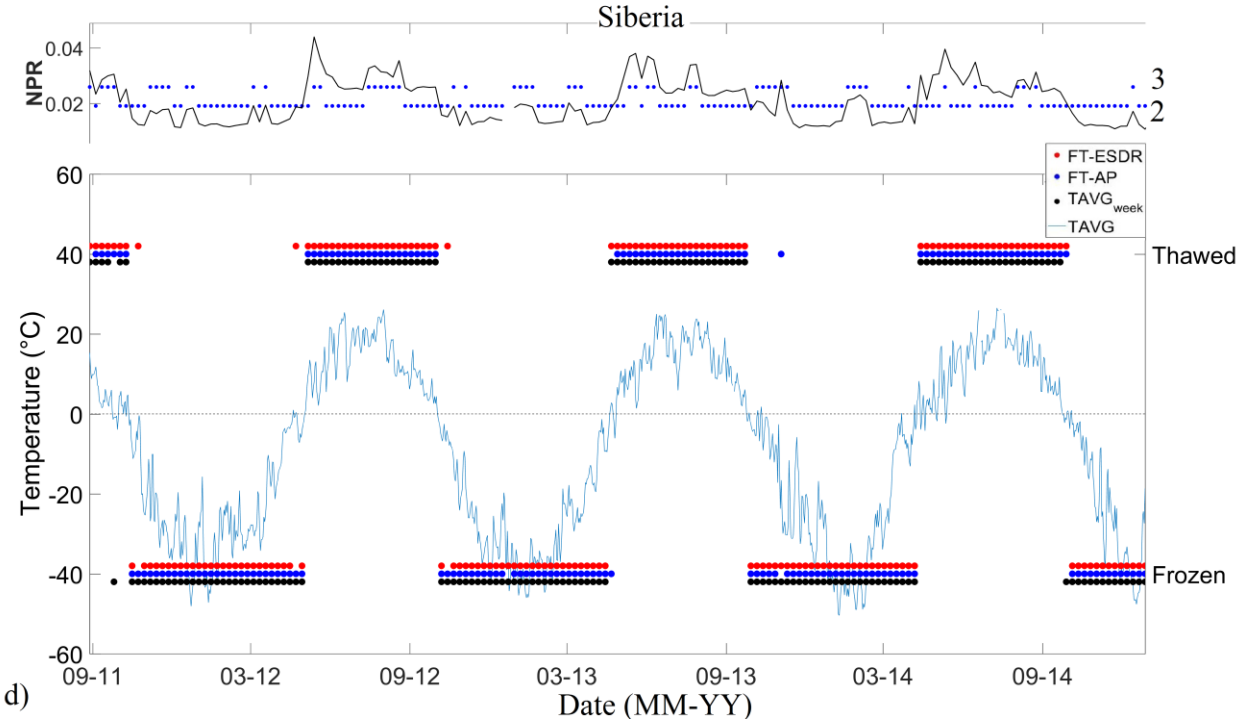
Siberia
NPR
0.04
0.02
3
2
FT-ESDR
FT-AP
TAVG week
TAVG
60
40
20
0
-20
-40
-60
Thawed
Frozen
Temperature (°C)
09-11
03-12
09-12
03-13
09-13
03-14
09-14
Date (MM-YY)

d)

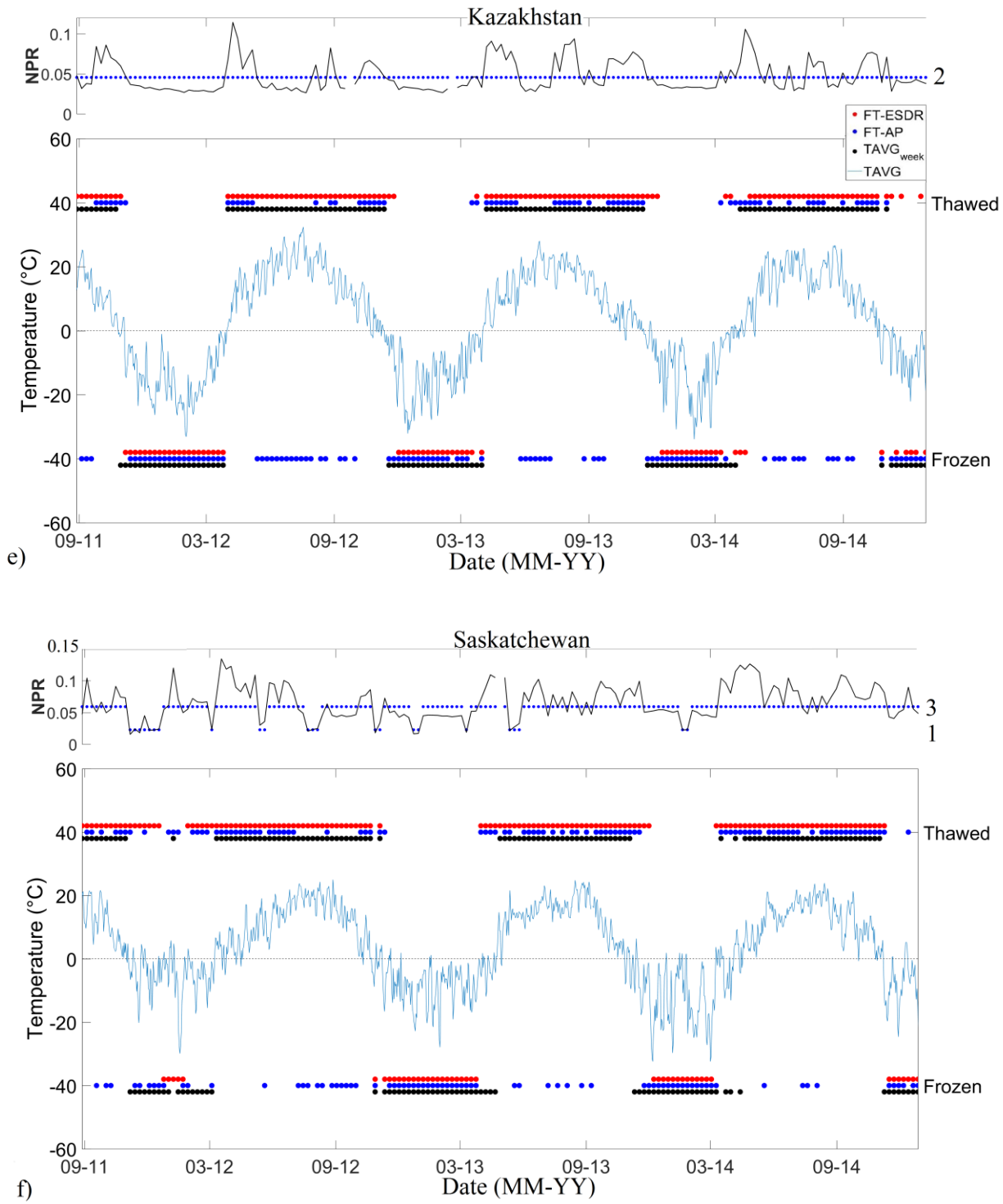

Figure 6. FT detection for each reference site (see Table 2), with FT-ESDR (red dots) and FT-AP (blue dots) against surface air temperature (black dots and blue line) in a) Kamchatka, b) Quebec, c) Alaska, d) Siberia, e) Kazakhstan and f) Saskatchewan. NPR series (top) contain the combination of available Aquarius observations following the prioritization of radiometer 2, radiometer 1 and then radiometer 3 (sect. 2.1). NPR threshold values (blue dot) according to Eq.1 with the corresponding beam number showed on the right.

Comparing both products to SAT at different sites shows that FT-AP tends to identify false frozen retrieval in summer periods. It is out of the scope of this paper to explain why these misclassifications occur, but some hypotheses will be given in Sect. 4.

4. Discussion

This study shows that overall FT-AP agrees well with weekly averaged SAT and with the Ka-Band FT-ESDR. Despite its being a weekly product, FT-AP has good sensitivity to the FT state of the landscape. Despite some regional discrepancies in forested landscape, very good agreements between FT-AP and FT-ESDR were found in this land cover, suggesting that the sensitivity of L- and Ka-bands to FT are more similar in forested landscape.

However, the study reveals that in certain regions, FT-AP seems to give false identifications of freezing surface in summer. These findings concord with other L-band FT analyses using SMAP and SMOS (Derksen et al., 2017; Rautiainen et al., 2016). Some regions like the coastlines, Kamchatka, Kazakhstan, Scandinavia, northern Europe, Alaska, the Canadian Rockies and the Canadian Prairies show agreement below 80% between FT-AP and FT-ESDR. An attempt was made to explain the false frozen retrievals occurring in the Kamchatka site and the two open land sites by looking at the Δ_{NPR} values, but no direct relationship was observable. Relatively small Δ_{NPR} are found for Kamchatka, but they are similar to those of Siberia, which has agreement higher than 95% with $TAVG_{week}$. The Alaska site has the smallest Δ_{NPR} of all the sites but does not possess the false frozen retrieval problem. To the contrary, the open land sites have the highest Δ_{NPR} values and both have frozen retrievals during summer. Hence, Δ_{NPR} can explain some of the weak classifications, but not all of them.

The false freeze classification in open land regions could be related to the crop growth cycle. The growing vegetation leads to a stronger emission from the vegetation in both horizontal and vertical polarization (Gherboudj et al., 2012), causing a depolarization of the signal that decreases the NPR. This creates a similar effect to the FT signal and could lead to false freeze identifications in summer (Roy et al., 2015; Rautiainen et al., 2016). Another important factor that could influence the precision of L-band FT retrieval is the possibility of low soil moisture before freezing. Since the FT retrieval is based on $\Delta\varepsilon_{ice/water}$, low soil moisture will lead to a low FT signal. Hence, in dry regions and where there is irrigation only during the growing season like

in Kazakhstan and the Canadian Prairies, dry soil could be misclassified as frozen soil as it has low permittivity.

Moreover, the different initial footprints of the analysed datasets could also explain some differences between them. For example, coastline proximity likely played a role in the Kamchatka results. Even if the products were resampled at the same scale, the surface heterogeneity such as the fraction of water (lakes and water near coastlines) within the initial footprint could generate changes in FT signals. In mountainous regions, it is possible that intra-pixel freeze onset date variability exists caused by colder temperatures at higher altitudes in contrast to warmer temperatures at lower altitudes. In this case, the frozen detections in some summer periods could be concurred with real freezing.

Putting aside those areas, the intercomparison shows recurrent patterns in the global annual freezing and thawing periods. A two to five week freeze onset delay is observed in tundra regions every year. Since this pattern is not as clearly seen as in forested area, it is unlikely that the differences come from the algorithm (i.e. STA vs MSTA methods). The causes are likely related to the physical behavior of microwave emissions at different frequencies, such as differences in emission and sensing depth, vegetation effects (as discussed previously) and ice/snow cover. Rowlandson et al. (2018) and Roy et al. (2017b) showed that L-band is sensitive to the freezing of the very surface related to the strong dielectric discontinuity, while the 37 GHz TB sensitivity is more related to the land surface temperature variation (Kim et al., 2017a). Hence, it is possible that the higher contrast of ice/water permittivity of L-band would make it more sensitive to the water-ice transition over the large landscape of a pixel (Artemov and Volkov, 2014; Roy et al. 2015; Rautianen et al., 2012, 2014). However, it remains that both FT products have different algorithms that could also lead to discrepancies. The FT-AP product looks at polarization ratio information, and its calibration is based on the land cover type. On the other hand, FT-ESDR is optimized pixel by pixel using single polarization observations at 37 GHz based primarily on the temperature information. Hence, further detailed ground-based measurements of soil state with radiometric emission at both frequencies could help to better differentiate these effects.

Soil heterogeneity makes the comparison with a single punctual in situ SAT limited (McColl et al., 2016; Lyu et al., 2018). While SAT is an indirect way to derive information on soil FT state, it was used in this study because it is a more homogenous reference than soil temperature. Soil temperature influences the emission (by Planck's law) of landscape elements such as soil, snow and vegetation. Moreover, L-band TB are also sensitive to soil moisture (see the review from Wigneron et al., 2017) which could have strong spatial variability at local scale. Microwave emissions detected by a satellite radiometer with all the spatial variability of the environment within a pixel cannot be solely validated by SAT, since it does not consider phenomena like soil thermal inertia and latent heat exchange.

5. Data availability

The FT-AP is archived and distributed by the NASA Distributed Active Archive Center of the National Snow and Ice Data Center (NSIDC DAAC). The FT-AP can be accessed through the NSIDC online public data server (https://nsidc.org/data/aq3_ft/versions/5). Table 6 summarizes all the datasets used in this study and lists where they are available for download.

Table 6: Product name, citation and URL for each dataset used in this study

Product name	Citation	URL
Aquarius TB weekly Level-3 L-Band	Brucker et al., 2015	https://nsidc.org/data/AQ3_TB/versions/5
EASE-Grid 2.0	Brodzik et al., 2014	https://nsidc.org/data/ease/ease_grid2.html
FT-ESDR	Kim et al., 2017b	https://nsidc.org/data/nsidc-0477/versions/4
Land cover LCC_{BU}	Brodzik *and* Knowles, 2011	https://nsidc.org/data/nsidc-0610/versions/1
Weather stations		https://www.ncdc.noaa.gov/cdo-web/datasets
Ruggedness	Gruber 2012	http://www.geo.uzh.ch/microsite/cryodata/pf_global

6. Conclusion

In recent years, more attention has focussed on the use of satellite observations to retrieve surface freeze/thaw state. The new FT product derived from L-Band Aquarius passive observations (FT-AP) ensures, with the still operating SMAP mission, an L-band passive FT monitoring continuum

with NASA's spaceborne radiometers, for a period beginning in August 2011. In this study, we evaluated the FT-AP and compared it with a product based on 37 GHz measurements (FT-ESDR). This investigation has shown that FT-AP was generally good at retrieving the FT state of the surface for the given time of Aquarius mission, as 77.1% of the common grid cells have more than 80% agreement with FT-ESDR. Differences between the FT-AP and FT-ESDR occur during the complex transitional freezing and thawing periods. The comparison with in situ daily surface air temperature (SAT) showed cases of good concordance with FT-AP and station measurements during those periods. It was also shown that false frozen retrievals in summer with FT-AP also lead to discrepancies between both products. The problem can be caused by surface properties such as vegetation and low soil moisture that influence the L-band NPR.

The study showed that differences between FT products can be caused by the response of frequency to the component in a pixel like vegetation, soil, snow, footprint size. Deeper analysis of multi-frequency differences in relation to FT retrieval is needed. Hence, our results open the path to look at the fusion of multi-frequency algorithms for FT retrievals from passive microwave satellite observations and upcoming missions like the Water Cycle Observation Mission (WCOM; Shi et al., 2016).

Competing interests. The authors declare that they have no conflict of interest.

Acknowledgments

The authors would like to thank the Canadian Space Agency (CSA) and the National Sciences and Engineering Research Council of Canada (NSERC) for their financial support. L. Brucker was supported by NASA Interdisciplinary Research in Earth Science (IDS).

References

Artemov, V. G. and Volkov, A. A.: Water and Ice Dielectric Spectra Scaling at 0°C, Ferroelectrics, 466(1), 158–165, doi:10.1080/00150193.2014.895216, 2014.

Barr, A., Black, T. A. and Mccaughey, H.: Climatic and phenological controls of the carbon and energy balances of three contrasting boreal forest ecosystems in western Canada, in *Phenology of Ecosystem Processes,* A. Noormet., P. of E. Processes., 2009.

Black, T. A., Nesic, Z., Chen, Z., Chen, W. J., Barr, A. G., Arain, M. A., Neumann, H. H. and Yang, P. C.: Increased carbon sequestration by a boreal deciduous forest in years with a warm spring, Geophys. Res. Lett., 27(9), 1271–1274, 2000.

Brodzik, M. J. and K. Knowles. *EASE-Grid 2.0 Land Cover Classifications Derived from Boston University MODIS/Terra Land Cover Data, Version 1*. [Subset used: 36 km, all land classes]. Boulder, Colorado USA. NASA National Snow and Ice Data Center Distributed Active Archive Center. doi: https://doi.org/10.5067/XR8523MC24TB, 2011

Brodzik, M. J., Billingsley B., Haran T., Raup B., Savoie M. H. *Correction: Brodzik, M. J. et al. EASE-Grid 2.0: Incremental but Significant Improvements for Earth-Gridded Data Sets*. ISPRS International Journal of Geo-Information 2012, 1, 32-45. ISPRS International Journal of Geo-Information, 3(3):1154-1156, doi:10.3390/ijgi3031154, 2014

Brucker, L., E. Dinnat, and L. Koenig. 2015. *Aquarius L3 Weekly Polar-Gridded Brightness Temperature and Sea Surface Salinity, Version 5*. [Subset used: Northern Hemisphere (NH), beam 1, 2 and 3]. Boulder, Colorado USA. NASA National Snow and Ice Data Center Distributed Active Archive Center. doi: https://doi.org/10.5067/Aquarius/AQ3_TB.005.

Brucker, L., Dinnat, E. P. and Koenig, L. S.: Weekly gridded Aquarius L-band radiometer/scatterometer observations and salinity retrievals over the polar regions - Part 1: Product description, The Cryosphere, 8(3), 905–913, doi: 10.5194/tc-8-905-2014, 2014.

Derksen, C., Xu, X., Scott Dunbar, R., Colliander, A., Kim, Y., Kimball, J. S., Black, T. A., Euskirchen, E., Langlois, A., Loranty, M. M., Marsh, P., Rautiainen, K., Roy, A., Royer, A. and Stephens, J.: Retrieving landscape freeze/thaw state from Soil Moisture Active Passive (SMAP) radar and radiometer measurements, Remote Sens. Environ., 194, 48–62, doi:10.1016/j.rse.2017.03.007, 2017.

Gherboudj, I., Magagi, R., Goïta, K., Berg, A. A., Toth, B. and Walker, A.: Validation of SMOS Data Over Agricultural and Boreal Forest Areas in Canada, IEEE Trans. Geosci. Remote Sens., 50(5), 1623–1635, 2012.

Gouttevin, I., Menegoz, M., Dominé, F., Krinner, G., Koven, C., Ciais, P., Tarnocai, C. and Boike, J.: How the insulating properties of snow affect soil carbon distribution in the continental pan-Arctic area, J. Geophys. Res. Biogeosciences, 117(2), 1–11, doi:10.1029/2011JG001916, 2012.

Gray, D.M.; Landine, P.G.; Granger, R. J.: Simulating infiltration into frozen Prairie soils in streamflow models, Can. J. Earth Sci., 22, 464–472, 1984.

Gruber, S.: The Cryosphere Derivation and analysis of a high-resolution estimate of global permafrost zonation, The Cryosphere, 6, 221–233, doi:10.5194/tc-6-221-2012, 2012.

Hallikainen, M. T., Ulaby, F. T. and Mohamed, A.: Dielectric Properties of Snow in the 3 to 37 GHz, IEEE Trans. Antennas Propag., AP-34(11), 1329–1340, doi:0018-926X/86/1100-1329, 1986.

IPCC, 2014: Climate Change 2014: Synthesis Report. Contribution of Working Groups I, II and III to the Fifth Assessment Report of the Intergovernmental Panel on Climate Change [Core Writing Team, R.K. Pachauri and L.A. Meyer (eds.)]. IPCC, Geneva, Switzerland, 151 pp, 2014

Kim, Y., Kimball, J. S., McDonald, K. C. and Glassy, J.: Developing a global data record of daily landscape freeze/thaw status using satellite passive microwave remote sensing, IEEE Trans. Geosci. Remote Sens., 49(3), 949–960, doi:10.1109/TGRS.2010.2070515, 2011.

Kim, Y., Kimball, J. S., Zhang, K. and McDonald, K. C.: Satellite detection of increasing Northern Hemisphere non-frozen seasons from 1979 to 2008: Implications for regional vegetation growth, Remote Sens. Environ., 121, 472–487, doi:10.1016/j.rse.2012.02.014, 2012.

Kim, Y., Kimball, J. S., Glassy, J. and Du, J.: An extended global Earth system data record on daily landscape freeze – thaw status determined from satellite passive microwave remote sensing, Earch Syst. Sci. Data, 133–147, doi: 10.5194/essd-9-133-2017, 2017a.

Kim, Y., Kimball, J. S., Glassy, J. and McDonald., K. C.: MEaSUREs Global Record of Daily Landscape Freeze/Thaw Status, Version 4 [Subset used: SSMI_37V_CO_FT_xxxx_dayxxx_v04.h5]. NASA National. Snow Ice Data Center Distributed Active Archive Center, Boulder, Colorado. doi: http://dx.doi.org/10.5067/MEASURES/CRYOSPHERE/nsidc-0477.004, 2017b.

Kumar, N., Grogan, P., Chu, H., Christiansen, C. T., Walker, V. K. and Sciences, M.: The Effect of Freeze-Thaw Conditions on Arctic Soil Bacterial Communities, Biology (Basel), 2, 356–377, doi:10.3390/biology2010356, 2013.

Kurganova, I., Teepe, R. and Loftfield, N.: Influence of freeze-thaw events on carbon dioxide emission from soils at different moisture and land use, Carbon Balance Manag., 9, 1–9, doi: 10.1186/1750-0680-2-2, 2007.

Langer, M., Westermann, S., Heikenfeld, M., Dorn, W. and Boike, J.: Remote Sensing of Environment Satellite-based modeling of permafrost temperatures in a tundra lowland landscape, Remote Sens. Environ., 135, 12–24, doi:10.1016/j.rse.2013.03.011, 2013.

Lyu, H., McColl, K. A., Li, X., Derksen, C., Berg, A., Black, T. A., Euskirchen, E., Loranty, M., Pulliainen, J., Rautiainen, K., Rowlandson, T., Roy, A., Royer, A., Langlois, A., Stephens, J., Lu, H. and Entekhabi, D.: Validation of the SMAP freeze/thaw product using categorical triple collocation, Remote Sens. Environ., 205, 329–337, doi:10.1016/j.rse.2017.12.007, 2018.

McColl, K. A., Roy, A., Derksen, C., Konings, A. G., Hamed, S. and Entekhabi, D.: Triple collocation for binary and categorical variables: Application to validating landscape freeze / thaw retrievals, Remote Sens. Environ., 176, 31–42, doi:10.1016/j.rse.2016.01.010, 2016.

Panneer Selvam, B. P., Laudon, H., Guillemette, F. and Berggren, M.: Influence of soil frost on the character and degradability of dissolved organic carbon in boreal forest soils, J. Geophys. Res. Biogeosciences Res., 829–840, doi:10.1002/2015JG003228.Received, 2016.

Peng, X., Frauenfeld, O. W., Cao, B., Wang, K., Wang, H., Su, H., Huang, Z., Yue, D. and Zhang, T.: Response of changes in seasonal soil freeze/thaw state to climate change from 1950 to 2010 across china, J. Geophys. Res. Earth Surf., (121), 1984–2000, doi:10.1002/2016JF003876, 2016.

Poutou, E., Krinner, G. and Genthon, C.: Role of soil freezing in future boreal climate change, Clim. Dyn., (23), 621–639, doi:10.1007/s00382-004-0459-0, 2004.

Rautiainen, K., Lemmetyinen, J., Pulliainen, J., Vehvilainen, J., Drusch, M., Kontu, A., Kainulainen, J. and Seppänen, J.: L-band radiometer observations of soil processes in boreal and subarctic environments, IEEE Trans. Geosci. Remote Sens., 50(5 PART 1), 1483–1497, doi:10.1109/TGRS.2011.2167755, 2012.

Rautiainen, K., Lemmetyinen, J., Schwank, M., Kontu, A., Ménard, C. B., Mätzler, C., Drusch, M., Wiesmann, A., Ikonen, J. and Pulliainen, J.: Detection of soil freezing from L-band passive microwave observations, Remote Sens. Environ., 147, 206–218, doi:10.1016/j.rse.2014.03.007, 2014.

Rautiainen, K., Parkkinen, T., Lemmetyinen, J., Schwank, M., Wiesmann, A., Ikonen, J., Derksen, C., Davydov, S., Davydova, A., Boike, J., Langer, M., Drusch, M. and Pulliainen, J.:

SMOS prototype algorithm for detecting autumn soil freezing, Remote Sens. Environ., 180, 346–360, doi:10.1016/j.rse.2016.01.012, 2016.

Rowlandson, T., A. Berg, A., Roy, A., Kim, E., Pardo Lara, R., Powers, J., Lewis, K., Houser, P., McDonald, K., Toose, P., Wu, A., De Marco, E., Derksen, C., Entin, J., Colliander, A. and Xu Xiaolan: Capturing Agricultural Soil Freeze/Thaw State through Remote Sensing and Ground Observations: A Soil Freeze/Thaw Validation Campaign, Remote Sens. Environ., 211, 59-70, doi:10.1016/j.rse.2018.04.003, 2018.

Roy, A., L. Brucker, M. Prince, A. Royer, and C. Derksen. Aquarius L3 Weekly Polar-Gridded Landscape Freeze/Thaw Data, Version 5. [Indicate subset used]. Boulder, Colorado USA. NSIDC: National Snow and Ice Data Center. doi: https://doi.org/10.5067/OV4R18NL3BQR, 2018

Roy, A., Royer, A., Derksen, C., Brucker, L., Langlois, A., Mialon, A. and Kerr, Y. H.: Evaluation of Spaceborne L-Band Radiometer Measurements for Terrestrial Freeze/Thaw Retrievals in Canada, IEEE J. Sel. Top. Appl. Earth Obs. Remote Sens., 8(9), 4442–4459, doi:10.1109/JSTARS.2015.2476358, 2015.

Roy, A., Id, P. T., Derksen, C., Rowlandson, T., Berg, A., Lemmetyinen, J., Royer, A., Tetlock, E., Helgason, W. and Sonnentag, O.: Spatial Variability of L-Band Brightness Temperature during Freeze / Thaw Events over a Prairie Environment, Remote Sens., 9(894), 1–16, doi:10.3390/rs9090894, 2017a.

Roy, A., Toose, P., Williamson, M., Rowlandson, T., Derksen, C., Royer, A., Berg, A. A., Lemmetyinen, J. and Arnold, L.: Response of L-Band brightness temperatures to freeze/thaw and snow dynamics in a prairie environment from ground-based radiometer measurements, Remote Sens. Environ., 2017b.

Schaeffer, Kevin; Zhang, Tingjun, Bruhwiler, Lori; Barrett, A. P.: Amount and timing of permafrost carbon release in response to climate warming, Tellus, 63B, 165–180, doi:10.1111/j.1600-0889.2011.00527.x, 2011.

Schwank, M., Stähli, M., Wydler, H., Leuenberger, J., Mätzler, C., Member, S. and Flühler, H.: Microwave L-Band Emission of Freezing Soil, IEEE Trans. Geosci. Remote Sens., 42(6), 1252–1261, 2004.

Ulaby, F. T., Moore, R. K. and Fung, A. K.: Microwave remote sensing: active and passive. Volume III: from theory to applications, Remote Sen., Artech House., 1986.

Shi, J., Dong, X., Zhao, T., Du, Y., Liu, H., Wang, Z., Zhu, D., Xiong, C., Jiang, L., Shi, J. and Dong, X.: The Water Cycle Observation Mission (WCOM): Overview, In Proceedings of the Geoscience and Remote Sensing Symposium (IGARSS), Beijing, China, 3430–3433, 2016.

Wigneron, J., Jackson, T. J., Neill, P. O., Lannoy, G. De, Rosnay, P. De, Walker, J. P., Ferrazzoli, P., Mironov, V., Bircher, S., Grant, J. P., Kurum, M., Schwank, M., Munoz-sabater, J., Das, N., Royer, A., Al-yaari, A., Bitar, A. Al, Fernandez-moran, R., Lawrence, H., Mialon, A., Parrens, M., Richaume, P., Delwart, S. and Kerr, Y.: Modelling the passive microwave signature from land surfaces : A review of recent results and application to the L-band SMOS & SMAP soil moisture retrieval algorithms, Remote Sens. Environ., 192(January), 238–262, doi:10.1016/j.rse.2017.01.024, 2017.

Xu, L., Myneni, R. B., Iii, F. S. C., Callaghan, T. V, Pinzon, J. E., Tucker, C. J., Zhu, Z., Bi, J., Ciais, P., Tømmervik, H., Euskirchen, E. S., Forbes, B. C., Piao, S. L., Anderson, B. T., Ganguly, S., Nemani, R. R., Goetz, S. J., Beck, P. S. A., Bunn, A. G., Cao, C. and Stroeve, J. C.: Temperature and vegetation seasonality diminishment over northern lands, Nat. Clim. Chang., (March), 1–6, doi:10.1038/nclimate1836, 2013.

Zheng, D., Wang, X., Velde, R. Van Der, Zeng, Y., Wen, J., Wang, Z., Schwank, M., Ferrazzoli, P., Member, S. and Su, Z.: L-Band Microwave Emission of Soil Freeze – Thaw Process in the Third Pole Environment, IEEE Trans. Geosci. Remote Sens., 55(9), 5324–5338, 2017.

3. Effets de la variabilité spatiale intra-pixel du gel/dégel de surface sur les mesures bande L du radiomètre satellitaire SMAP en forêt boréal

« Freeze/Thaw Intra-pixel Spatial Variability Effects on SMAP L-band Radiometer Measurements in Boreal Forest »

Michael Prince[1,2], Alexandre Roy[2,3], Alain Royer[1,2], Alexandre Langlois[1,2]

[1] Centre d'Applications et de Recherches en Télédétection (CARTEL), Université de Sherbrooke, Sherbrooke, QC J1K 2R1, Canada
[2] Centre d'Étude Nordique, Université Laval, Québec, Canada
[3] Département des Sciences de l'Environnement, Université du Québec à Trois-Rivières (UQTR), QC, Canada

Cet article a été soumis à *Remote Sensing of Environement*. Il est présentement en révision scientifique.

3.1 Présentation de l'article

L'analyse globale faite dans le premier article a démontré qu'il existe des différences dans les estimations du gel/dégel entre les produits satellitaires. Afin d'aider à mieux comprendre le comportement de la télédétection satellitaire du gel/dégel en bande L en forêt boréale, ce deuxième article regarde la problématique de l'hétérogénéité de l'environnement compris sous un pixel de résolution grossière (36 km) relié à la télédétection passive en bande L. L'étude montre qu'il y a une forte variabilité spatiale du gel du sol en forêt boréale qui est détectée par le radiomètre satellitaire de SMAP. Par ce constat, un algorithme est développé puis évalué permettant d'estimer un pourcentage de sol gelé intrapixel à partir des observations SMAP. Cet algorithme, qui est dérivé du produit gel/dégel de SMAP, permet d'améliorer ce dernier en transformant l'estimation qualitative binaire (gelé/dégelé) en une estimation quantitative sous forme de pourcentage de surface gelé. Cette méthode permettrait d'utiliser davantage l'information comprise dans les mesures du radiomètre satellitaire.

Le travail d'analyse et l'écriture de cet article ont été entièrement réalisés par moi-même dans le cadre de cette maîtrise, en incluant, de plus, une mission sur le terrain (Août 2017).

3.2 Article 2

Abstract

Soil surface temperature is one of the main WMO (*World Meteorological Organization*) Climate Essential Variables for monitoring the impact of climate variability in northern regions. To evaluate the spatial and temporal variability of the autumn freeze in northeastern Canada boreal forest, a network of compact and self-recording temperature sensors (iButton) along transects aeraging 10 km was deployed on the soil surface at two different sites. Results show important spatial variability in soil freezing timing with maximums, for the two sites, spanning from 7.5 to 9.5 weeks to reach a frozen state. It is known that L-band can monitor freeze/thaw (FT) seasonality at low spatial resolution (~40 km), but the effect of SMAP intra-pixel spatial variability of fall freezing had yet to be investigated and is thus addressed in this paper. Simulations of brightness temperature (TB) weighted by spatially distributed iButton FT records and using the ω-τ vegetation model show good agreement with SMAP satellite observations during the fall transition period with an average RMSE of 3.5 K. A new intra-pixel frozen soil percentage retrieval algorithm using only SMAP observations and air temperature is proposed. The percentage of frozen soil in falls 2015 and 2016 from the new algorithm and the in situ measurements are in good agreement with a coefficient of determination (R^2) ranging between 0.63 and 0.88.

1. Introduction

The seasonal freeze/thaw (FT) cycle affects over half the land surface of the northern hemisphere. The behaviour of FT transitions in the environment is characterized by high temporal and spatial variability, with measurable impacts on climate (IPCC, 2014; Peng et al., 2016; Poutou et al., 2004), hydrology (Gouttevin et al., 2012; Gray et al., 1985), ecology (Kumar et al., 2013; Black et al., 2000), biogeochemical processes (Selvam et al., 2016; Xu et al., 2013; McGuire et al., 2012; Schaefer et al., 2011) and permafrost at high latitudes (Schuur et al., 2015). In cold regions, the vegetation growing season is significantly correlated with the length of the spring thaw (Kim et al., 2012), while forest carbon balances fluctuate with the interannual variability of FT cycles (Barr et al., 2009; Kurganova et al., 2007). In the boreal forest, even if

higher temperatures extend the vegetation growing season, it is difficult to predict how this temperature increase will affect the ecosystem's net productivity. For example, CO_2 capture by photosynthesis in many boreal ecosystems is limited by decreased sunlight in fall. Warmer temperatures would thus produce a marginal increase in photosynthesis, but also an increase in respiration (Mahecha et al., 2010; Suni et al., 2003). Hence, better understanding and tracking how these cycles vary with climate warming is a key to understand the carbon balance in northern regions. However, temporal and spatial data on changes of the FT state of the soil in these regions is limited.

Spaceborne passive microwave sensors have proven effective at detecting soil FT state and have the advantage of providing global high temporal resolution measurements (under 3 days) of brightness temperature (TB) without being dependent on sunlight hours and with few atmospheric interactions (Prince et al., 2018; Rautiainen et al., 2016; Roy et al., 2015; Kim et al., 2011). L-band has characteristics favorable for remote FT detection, including a relatively high penetration (emission) depth (about 5 cm in thawed soil) and sharp contrast between the permittivity of water and ice ($\Delta\varepsilon_{water/ice}$), as demonstrated in many studies (Zheng et al., 2017; Roy et al., 2017a; Derksen et al., 2017; Rautiainen et al., 2014; 2012; Schwank et al., 2004).

One major drawback of passive L-band microwave remote sensing is its coarse spatial resolution. Environmental heterogeneity within pixels, including the frozen soil fraction, is a source of uncertainty when creating and using remote sensing products. This parameter can vary on a very small scale (Rowlandson et al., 2018; Roy et al., 2017a), making it difficult to link a discrete in situ measurement to its corresponding remote sensing pixel. However, the potential spatial variability of soil freezing that influences remote observations can be an opportunity to measure the evolution of fall soil freezing in remote environments such as the boreal forest. Roy et al. (2015) showed that for certain boreal forest sites, the FT signal is gradual in the fall, which could be related to the spatial variability of frozen soil. Another study showed that for an agricultural site, the Soil Moisture Active Passive radiometer (SMAP; 2015-present) is sensitive to the proportion of frozen soil within a pixel (Rowlandson et al., 2018). The challenge is to measure soil temperatures over several kilometers to assess the evolution of soil freezing and its impact on L-band radiometer observations.

The objectives of this paper were thus to: 1) assess the spatial variability of soil freezing in boreal forest using networks of ground temperature sensors; 2) verify the influence of the evolution of fall soil freezing on SMAP TB observations; and 3) develop an estimation algorithm for the intra-pixel percentage of frozen soil in SMAP radiometer observations.

2 Methodology

2.1 In situ data

To evaluate the spatial variability of fall soil freezing in boreal forest, temperature sensors (iButton; Lundquist and Lott, 2008) were installed at two different sites along transects several kilometers long. The first site is in the Baie-James – Le Moyne region (53.41° N -75.01° W; "BJ"), and the second is near Lac Chisapaw (54.97° N -76.31°W; 100 km east of Kuujjuarapik; "KJ"). The regions were selected to limit water bodies in the SMAP pixels and to analyze a typical Canadian taiga ecosystem dominated by black spruce (*Picea mariana*). At each site, iButtons were installed at ground level (0 cm) under the lichen along the two transects (Figure 1), with 14 points over 30 km at BJ (8 km + 22 km) and 13 points over 12 km at KJ (6 km + 6 km). Each iButton measures the temperature every 3 hours. The iButton locations were locally randomly selected to represent a variety of soil types and forest densities. They had to be accessible on foot via a trail defined by the landscape's geomorphology and natural obstacles. The distance between iButtons is about 1 km, except on the BJ north-south transect, where access to a logging road allowed distances of 3 km. At each site, two iButton devices were installed on tree trunks at breast height to measure the temperature of the vegetation (T_{veg}). In addition, each site was equipped with a weather station to measure the air temperature (T_{air}) at 2 m every 30 minutes. Note that a technical failure at the KJ weather station made it impossible to measure T_{air} from October 2015 to August 2016. This missing data was replaced with T_{veg} readings from the KJ iButtons, since T_{air} and T_{veg} are similar (Section 3.1).

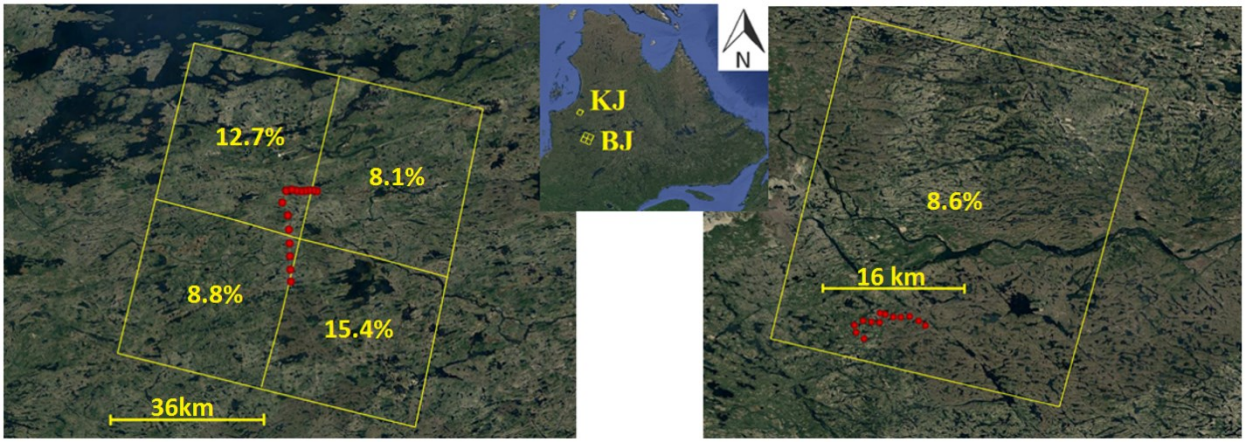

Figure 1: Baie-James – Le Moyne (BJ) site (Left) and Lac Chisapaw – Kuujjuarapik (KJ) site (Right) showing iButton locations (red dots). The yellow rectangles delineate SMAP pixels. The intra-pixel water percentage from the SMAP L1C file is given in the middle of each pixel. Background: Landsat images from Google Earth.

To determine their accuracy, the iButtons were submerged in a container of regularly-stirred ice water (0°C). The measurements gave an average of 0.210°C with a standard deviation of 0.046°C, within an interval between 0.143°C and 0.288°C. The accuracy of the iButtons is therefore on the order of 0.05°C with a slight positive bias of between 0.2 and 0.3°C. The spatial variability of fall soil freezing is quantified as a frozen soil fraction based on the T_{soil} time series using the approach detailed in Section 2.4.4. Dates when T_{soil} from each iButton drops below these thresholds are noted to measure the time required for all iButtons to detect frozen soil.

The diameter at breast height (DBH) of all trees (all black spruce) within a 5 m radius of each iButton was measured. Using the DBH, the wood volume was estimated with the Ter-Mikaelian and Korzukhin (1997) equations and an average dry wood density of 450 kg m^{-3} for black spruce. Lichen, litter and organic soil depths were measured at each iButton location, and a soil sample was collected for particle size analysis using the Mériaux (1954) density method and the Canada Soil Survey Committee classification (1987). Table 1 summarizes the characteristics of each location. The characteristics were analyzed to determine whether they had an impact on the variability of the freeze onset date.

.

Table 1: Coordinates, Stem Volume and Soil Characteristics for each iButton.

iButton	Latitude (°N)	Longitude (°W)	Stem volume (m^3/ha)	Lichen (cm)	Litter (cm)	Organic soil (cm)	Granulometric Class
BJ1	53.381	-75.031	30.95	5-6	4-5	10	Organic
BJ2	53.354	-75.014	75.06	8-10	1-2	3-5	Loamy Sand
BJ3	53.322	-75.012	69.8	5	4-5	6	-
BJ4	53.293	-75.012	17.00	4-5	4-5	6	Loam
BJ5	53.265	-75.012	85.06	10-12	4-5	4-5	Sandy Loam
BJ6	53.236	-75.013	41.79	2-4	1	4-5	Sandy Loam
BJ7	53.211	-75.014	19.92	5-6	5	12-13	Organic
BJ8	53.408	-74.993	54.15	8-10	6	4-5	Loamy Sand
BJ9	53.405	-74.977	17.65	2-3	4	10	Sandy Loam
BJ10	53.404	-74.961	64.93	1	10	31	Sandy Loam
BJ11	53.404	-74.947	3.85	4-6	4	5-6	Sandy Loam
BJ12	53.405	-74.931	23.51	5-7	4-5	1	Sandy Loam
BJ13	53.404	-74.917	0.00	3	4	2-3	Sandy Loam
BJ14	53.402	-74.904	0.66	4-5	4-5	4	Sandy Loam
KJ1	54.972	-76.305	0.00	3	0	3	Loamy Sand
KJ2	54.969	-76.291	0.00	0-1	0	2	Loamy Sand
KJ3	54.969	-76.278	0.00	3-4	2-3	8	Organic
KJ4	54.969	-76.262	0.00	2-3	3-4	7	Organic
KJ5	54.964	-76.246	0.00	1-2	2-3	6-7	Sandy Loam
KJ6	54.959	-76.235	73.17	1-2	2-3	6-7	Organic
KJ7	54.972	-76.305	0.00	-	-	-	Swamp
KJ8	54.964	-76.316	41.28	4-5	1-2	6-7	Sandy Loam
KJ9	54.965	-76.330	26.20	4-6	3-4	18	Organic
KJ10	54.966	-76.345	111.80	3-4	1-2	6-7	Organic
KJ11	54.962	-76.360	41.90	2-3	2	3-4	Loamy Sand
KJ12	54.954	-76.358	38.19	2	2	2-3	Loamy Sand
KJ13	54.948	-76.34	43.18	4-5	2-3	4	Sandy Loam

2.2 SMAP brightness temperature data

The horizontally (H) and vertically (V) polarized TB (TB_{SMAP}) measurements are from the SMAP L1C product on the Northern EASE-Grid 2.0 projection at 36 km x 36 km resolution (Chan et al., 2016). Data from descending (morning; average 06:50 EST) and ascending (afternoon; average 17:20 EST) SMAP overpasses were used. At the latitude of the study sites, SMAP takes one and occasionally two measurements per day. As shown in Figure 1, all iButton locations at KJ are within a single pixel. Conversely, at BJ, where locations are distributed across four pixels, only the measurements from the lower left pixel were used since it contained fewer bodies of water than the upper left pixel (where the most iButtons were located) and it possesses more iButtons than the upper right pixel.

2.3 Supplementary data

Land cover information was obtained from EASE-Grid 2.0 Land Cover Classifications derived from Boston University MODIS/TERRA Land Cover Data, Version 1 (LCC_{BU}) at 36 km resolution and in northern hemisphere projection (Brodzik and Knowles, 2011; NSIDC: nsidc.org/data/nsidc-0610/versions/1). The product uses the 17 International Geosphere Biosphere Programme land cover classes. For each site's representative pixel, it provides the percentage of each class based on the original MODIS/TERRA (MOD12Q1) product at 1 km resolution (Table 2).

Table 2: Percentage of each non-zero class from the LCC_{BU} for BJ and KJ pixels.

Class Number	Category	BJ (%)	KJ (%)
1	Evergreen needleleaf forest	6	0
5	Mixed forests	6	0
7	Open shrublands	35	61
8	Woody savannas	36	26
10	Grasslands	11	8
17	Water bodies	6	5

The Normalized Difference Vegetation Index (NDVI) used in this study is from MODIS/AQUA Vegetation Indices 16-Day L3 Global 1km (MYD13A2; Didan K., 2015). Pixels located in the

BJ and KJ pixels were selected by the nearest neighbor method. For each date, the average NDVI value was calculated to obtain a single NDVI value per SMAP pixel ([0.55 - 0.74] for BJ and [0.47 - 0.65] for KJ). A single NDVI value was needed for the simulation for each site and each freezing period beginning (see section 2.4.2). Thus, daily NDVI values were linearly interpolated from the 16-day values to approximate a value when required.

2.4 Brightness temperature simulation with the ω-τ model

2.4.1 ω-τ model

The ω-τ radiative transfer model (Mo et al., 1982) was used to quantify the effect of frozen soil on L-band emissions at the scale of an SMAP pixel in partially forest covered taiga. To simulate brightness temperature (TB_{sim}; Eq. 1) in a specific polarization (p) during fall FT transition periods, a TB with characteristics of frozen soil (TB_{fro}) was combined with a TB with characteristics of thawed soil (TB_{tha}) in proportion to the frozen soil fraction (F_{fro}) estimated by the iButtons (Eq. 7; see Section 2.4.4). The difference between TB_{tha} and TB_{fro} was primarily caused by the high $\Delta\varepsilon_{water/ice}$.

$$TB_{sim}(p) = F_{fro} * TB_{fro}(p) + (1 - F_{fro}) * TB_{tha}(p) \quad (1)$$

The ω-τ radiative transfer model (Mo et al., 1983) was used to simulate a polarization-dependent TB as a function of the effective soil temperature (T_{soil}) and vegetation temperature (T_{veg}) measured by the iButtons (Eq. 2). Equation 2 assumes that the atmosphere (Pellarin et al., 2016) and the snow cover (Roy et al., 2017b) are transparent to L-band emissions. To obtain the best comparison of TB_{sim} and TB_{SMAP}, only the iButton measurements closest in time to the SMAP overpasses were selected. Thus, T_{soil} and T_{veg} values are within a ±1.5 hr interval of their corresponding SMAP values.

$$TB_p = (1 - \Gamma_p)\gamma_p T_{soil} + (1 - \omega_p)(1 - \gamma_p)T_{veg} + \gamma_p\Gamma_p(1 - \omega_p)(1 - \gamma_p)T_{veg} \quad (2)$$

where Γ_p is the soil reflectivity, ω_p is the effective albedo and γ_p is the vegetation transmissivity. These three theoretically polarization-dependent parameters are effective parameters over a whole SMAP pixel (Wigneron et al., 2007). Furthermore, according to Wigneron et al. (2017),

since polarization effects are low, we can assume that $\gamma_H = \gamma_V = \gamma$ and that $\omega_H = \omega_V = \omega = 0.05$. Considering T_{veg} and T_{soil} to be known, this gives a system of two equations and three variables for each FT state (Eq. 3 and Eq. 4).

$$TB_{H.sim} = (1 - \Gamma_H)\,\gamma T_{soil} + 0.95(1 - \gamma)T_{veg} + \gamma\Gamma_H 0.95(1 - \gamma)T_{veg} \quad (3)$$

$$TB_{V.sim} = (1 - \Gamma_V)\,\gamma T_{soil} + 0.95(1 - \gamma)T_{veg} + \gamma\Gamma_V 0.95(1 - \gamma)T_{veg} \quad (4)$$

where Γ_H, Γ_V, and γ are the parameters to determine to calculate TB_{sim}. These parameters are highly dependent on environmental conditions, particularly soil moisture and the FT state (soil and vegetation) due to the high value of $\Delta\varepsilon_{water/ice}$ in L-band. They were estimated using a minimum root mean square error (RMSE) inversion between TB_{sim} and TB_{SMAP} (Eq. 5). Many values of TB_{sim} were calculated with iterations of different combinations of Γ_H, Γ_V, and γ. Two inversions (one for thawed state and one for frozen state) were developed to estimate γ (see Sections 2.4.2 and 2.4.3). When a value of γ is retrieved in the system of equations (Eq. 3 and Eq. 4), the RMSE converges to a distinct minimum with certain values of Γ_H and Γ_V.

$$RMSE = \min\left[\sqrt{(TB_{H.sim} - TB_{H.SMAP})^2 + (TB_{V.sim} - TB_{V.SMAP})^2}\right] \quad (5)$$

Lastly, the TB_H and TB_V calculated from the optimizations are used to obtain the normalized polarization ratios (NPR; Eq. 6), which was compared with the NPR observed by SMAP. The NPR index is very sensitive to soil FT state and is used in L-band detection algorithms (Roy et al., 2015; Rautiainen et al., 2016; Derksen et al., 2017).

$$NPR = \frac{TB_V - TB_H}{TB_V + TB_H} \quad (6)$$

2.4.2 Vegetation transmissivity during thaw period

The estimation algorithm for vegetation optical thickness (τ) is drawn from the SMAP Algorithm Theoretical Basis Document (ATBD) (O'Neill et al., 2015). It uses a vegetation water content (VWC) function based on the NDVI and the IGBP land cover classification (Chan et al., 2013). In the algorithm, each IGBP land cover class has constant parameters (stem factor, albedo

diffusion and vegetation parameter) that differ from the other classes. The values of these parameters are given in a look-up table in O'Neill et al. (2015). To estimate a global γ for each site, the algorithm was run for each class present in the BJ and KJ pixels and weighted by their intra-pixel land cover percentage (Table 2). This approach was used to calculate daily γ, from which Γ_H and Γ_V could be deduced. During the fall freeze period, Γ_H, Γ_V and γ were set at the last values estimated prior to the start of freezing (Table 3). This technique cannot be used to estimate γ during the freeze period, since the NDVI no longer reflects the vegetation when there is snow cover (Huete et al., 1999).

Table 3: Γ_H, Γ_V and γ values used to compute thawed TB (TB_{tha}; Eq.1) for the first and the second freezing season for BJ and KJ

Season/Site	Γ_H	Γ_V	γ
1rst BJ	0,43	0,29	0,64
2nd BJ	0,45	0,30	0,60
1rst KJ	0,33	0,24	0,78
2nd KJ	0,34	0,23	0,78

2.4.3 Vegetation transmissivity during the freeze period

Using the assumption that freeze conditions remain constant for a full February day, the days when the SMAP radiometer took both AM and PM measurements were selected. Equations 3 and 4 were solved for the AM and PM periods to produce a system of four equations and three unknowns for the inversion technique (Eq. 5). This gave an interval of potential values of γ between 0.8 and 0.96 with their associated Γ_H and Γ_V. Minimum RMSE was at γ = 0.87 for BJ and γ = 0.88 for KJ (Table 4). Each winter was processed with this method and produced similar values from year to year and between the sites.

Table 4: Γ_H, Γ_V and γ values used to compute frozen TB (TB_{fro}; Eq.1) for both the first and the second freezing season for BJ and KJ. The values for each site are the same for both seasons.

Site	Γ_H	Γ_V	γ
BJ	0,12	0,08	0,87
KJ	0,13	0,08	0,88

2.4.4 Frozen soil fraction

To estimate the time-dependent frozen soil fraction using iButton measurements (F_{fro}; Eq.1), a two-threshold (T_1 and T_2) approach was needed to classify the soil FT state in relation to T_{soil}.

Using two thresholds makes it possible to represent the state in which water and ice coexist during latent heat transfer, a physical process that cannot be represented by a single frozen-or-thawed threshold. Each T_{soil} time series is attributed a daily value ($iButton_{fro}$) of 0 (thawed), 0.5 (half frozen, half thawed) or 1 (frozen) in relation to T_1 and T_2 (Eq.7).

$$\begin{aligned} &\text{Si} \quad T_{soil} > T_1, && iButton_{gel} = 0 \\ &\text{Si} \quad T_1 \geq T_{soil} > T_2, && iButton_{gel} = 0.5 \\ &\text{Si} \quad T_2 \geq T_{soil}, && iButton_{gel} = 1 \end{aligned} \tag{7}$$

F_{fro} for BJ and KJ corresponds respectively to the average of daily $iButton_{fro}$ values. In order to obtain T_1 and T_2, the minimum RMSE inversion technique (Eq. 5) was applied, iterating T_1 and T_2 (only BJ afternoon values from the first year) and Γ_H, Γ_V, and γ calculated using the methods described in Sections 2.4.2 and 2.4.3. The resulting values, $T_1 = 1.7°C$ and $T_2 = 0.3°C$, were then used for the other BJ periods and for KJ.

2.5 SMAP frozen soil percentage estimation algorithm

Having showed the influence of spatial variability on the SMAP signal (Section 3.2), an algorithm was developed for estimating the frozen percentage from SMAP radiometry. The algorithm was applied separately to TB_H, TB_V and NPR data. The first step of the algorithm determines the start of freezing, when the air temperature drops below 0°C, using weather station air temperature data. The lowest TB value from about one week after that date is selected (or the highest, in the case of NPR) as the reference for 100% thawed soil (ref_{min} for TB; ref_{max} for NPR). The reference for 100% frozen soil (ref_{max} for TB; ref_{min} for NPR) is the TB average for the month of February (completely frozen) of each year. The frozen soil percentage in a pixel ($\%fro_X$; X = H, V or NPR) was thus calculated in three ways (Eq. 8):

$$\text{a) } \%fro_{X=H\ or\ V} = \frac{TB_p - ref_{min}}{ref_{max} - ref_{min}} * 100, \quad \text{b) } \%fro_{NPR} = 100 - \frac{NPR - ref_{min}}{ref_{max} - ref_{min}} * 100 \tag{8}$$

This was calculated for each data point in the time series, from the first freeze day to the day $\%fro_X = 100\%$. Before each calculation, two criteria are applied. The first assigns a null value for

days when T_{air} is over 0°C. This masks significant drops in TB that are normally caused by the presence of water in snow following a thaw (Roy et al., 2017a). Water in the snow absorbs soil emissions, turning the snow cover opaque and obscuring soil state data. The second criterion assigns the previous $\%fro_X$ value to dates when TB drops by more than 10% of (ref_{max} – ref_{min}) over the previous day. This smoothes the $\%fro_X$ curves to represent the snow insulating effect (see Section 3.1), which causes soil freezing to be a gradual process without large daily fluctuations. The small daily TB variations measured by the SMAP radiometer can be due to other causes (radiometer footprint, vegetation, lakes, etc.).

3 Results and discussion

3.1 FT spatial variability

Figure 2 shows T_{soil} values from each iButton (top), T_{veg} and T_{air} readings (middle), and F_{fro} (bottom) estimated with the algorithm described in Section 2.4.4 for the BJ (left) and KJ (right) sites. T_{veg} and T_{air} have similar values (combined curves), showing that air temperature can be used to represent vegetation temperature. The T_{soil} values clearly demarcate when snow cover appears. As an insulator, snow attenuates the large daily variations in soil temperature. Once there is snow cover, T_{soil} slowly drops to the freezing state.

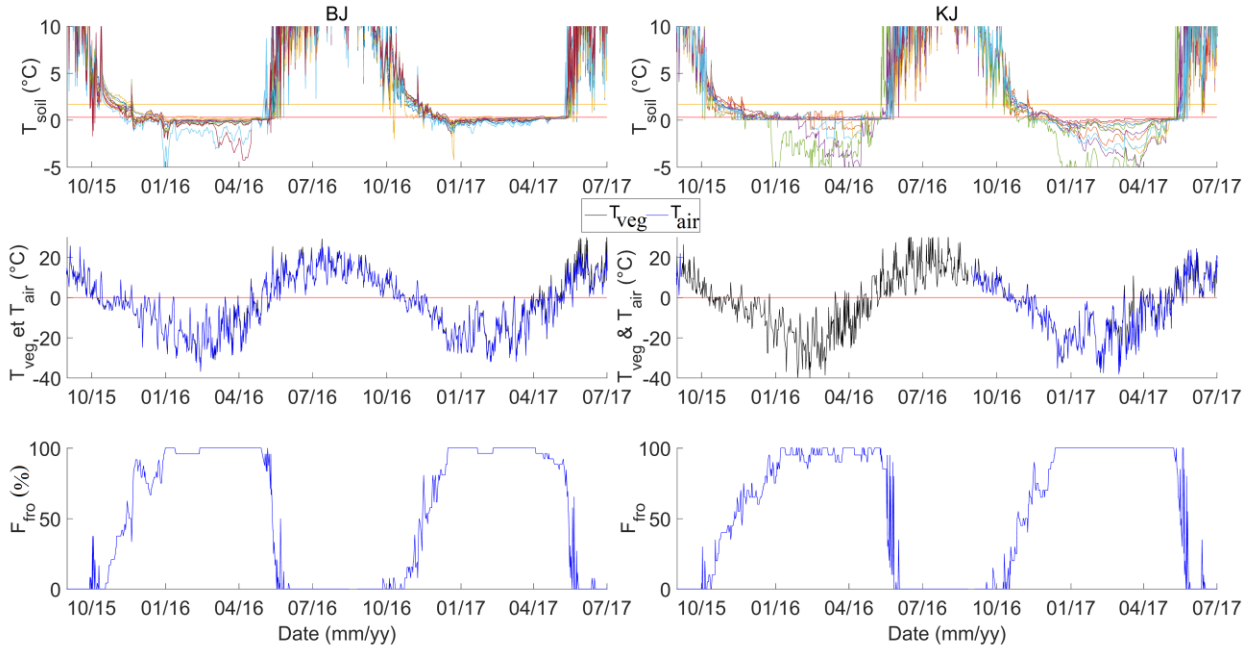

Figure 2: AM and PM (SMAP descending and ascending overpasses) soil temperature values (Tsoil) measured by the iButton units, with T1 and T2 thresholds represented by orange and red horizontal lines, respectively (top), vegetation and air temperatures, with 0°C represented by a red line (middle), and percentage of frozen soil from Ffro (bottom). BJ at left and KJ at right. The y-axes limits were fixed at -5°C to 10°C for T_{soil} graphs to zoom in the zones in interest where FT spatial variability is observable.

T_{soil} spatial variability in the freeze period can be seen in the time it takes for all T_{soil} to cross the T1 = 1.7°C and T2 = 0.3°C thresholds. For T1, this stretches over 5 and 5.5 weeks (BJ and KJ, respectively), and for T2, 7.5 to 9.5 weeks (BJ and KJ, respectively). During the freeze period, this difference translates into a gradual increase in F_{fro} variation curves until all soils are frozen, generally around the beginning of January. There is also a yearly difference in freeze period length. It lasted 98 days in 2016 and 83 days in 2017. During thaw periods, the T_{soil} cross the thresholds more spontaneously in groups, with a maximum timing difference of two weeks.

The correlation between freeze onset and wood volume, soil granulometric class, lichen layers, litter and mineral soil data was verified (data in Table 1). No significant correlation was found, except for a weak correlation with a coefficient of determination (R^2) of 0.26 ($p<0.006$) between the freeze onset date and stem volume. These results are considered in the discussion.

3.2 TB simulation during fall freeze periods

Figure 3 shows the TB_{sim} H and V time series produced using the method described in Section 2.4, compared to the TB_{SMAP} values. During FT periods, TB_{sim} values follow an increase/decrease pattern similar to SMAP. Wet snow events occurred during the first freeze period (11/15 to 01/16, 04/16 and 04/17), which are observable when there is a sharp drop in TB_{SMAP}. Those events are strongly correlated with T_{air} rising over 0°C (Fig. 2; middle), which means they consist of an absorption of microwave emissions by liquid water in the snowpack. Significant differences between TB_{sim} and TB_{SMAP} occur because this phenomenon is not considered by the TB_{sim} algorithm, while the SMAP radiometer is very sensitive to it (Roy et al., 2017b).

The root mean square error (RMSE) values shown on the graphs were calculated for each site and each polarization for a period from freeze start to the end of January of each year and masked when $T_{air} > 0$°C. Thus, the RMSE calculations ignore periods for which ω-τ parameters

were optimized (view Sections 2.4.2 and 2.4.3). The average RMSE is 3.5 K, with mostly lower values for the second year and for vertical polarization. The average RMSE is 4.6 K when the T_{air} > 0°C mask is removed. These results show good agreement between the simulation and SMAP measurements, which indicates that the spatial variability of fall freezing is a factor that has a significant influence on L-band emissions and that the SMAP radiometer is sensitive to the intra-pixel proportion of frozen soil.

There were also thaw events during the month of May 2017, when $TB_{H.SMAP}$ showed a drop not detected by $TB_{V.SMAP}$ or by TB_{sim}. These events are probably related to the formation of ice crust on the snow cover surface, which causes a drop in $TB_{H.SNAP}$ (Roy et al., 2015) but is not considered in TB_{sim}. During spring thaws, TB_{SMAP} readings drop significantly, and always before TB_{sim}. Once again, this is explained by the presence of water in the snow resulting from air temperatures above 0°C.

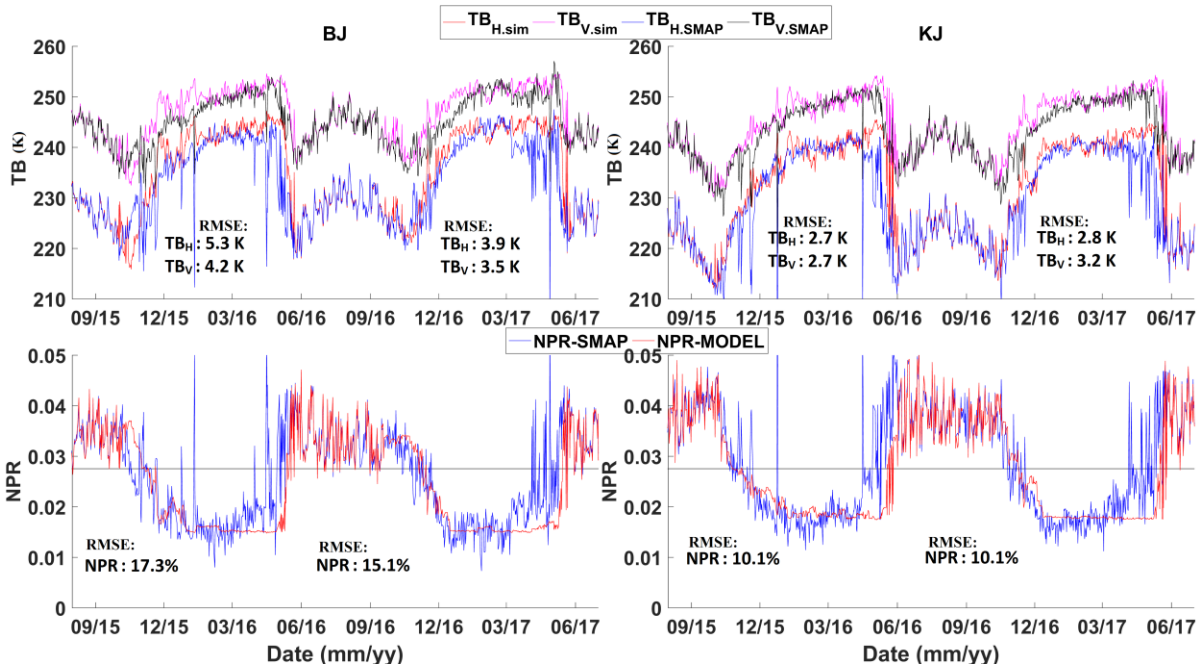

Figure 3: Time series of TBsim and TBSMAP AM and PM values (top), and NPRsim and NPRSMAP (bottom). RMSE values with snow mask applied for each freeze period are given below the curves. BJ at left and KJ at right.

The NPR time series behave similarly to the TB time series (Fig. 3; bottom). They show good concordance between model and satellite measurements, with relative RMSE values (in relation to the extent of its respective series) values, calculated during the freeze period, from 10.5% to

17.7%. The periods with major differences between the two curves correspond to the same wet snow and ice crust events described for the TB series. The black lines in Figure 3 indicate the FT thresholds calculated from the algorithm used by the current SMAP FT product (O'Neill et al., 2015). The algorithm estimates a surface thawed state for NPR values over the threshold and a frozen state for values below the threshold

3.3 Percentage frozen soil retrieval algorithm from SMAP

Given the sensitivity of SMAP to FT spatial variability shown in the previous section, an algorithm to estimate the percentage of frozen soil from SMAP ($\%fro_x$) was developed. Figure 4 compares the results of $\%fro_H$, $\%fro_V$ and $\%fro_{NPR}$ to F_{fro} results estimated by the iButtons (see Section 2.5). Missing data for $\%fro_x$ represent the freezing period have not started according or the presence of water in the snow, according to T_{air}. For the two frozen seasons at each site, scatter graphs of the points between $\%fro_x$ and F_{fro} were created, and the regression line slope (m), intercept (b) and R^2 are given in the tables in the lower right corner (Fig. 4). In general, all algorithms produce R^2 values of between 0.63 and 0.88, clearly showing that it is possible to measure the progression of intra-pixel frozen soil over a period of 9 weeks in the fall using SMAP observations. The $\%fro_{NPR}$ gives the best results (R^2 =0.74) at BJ and $\%fro_H$ gives the best results (R^2 = 0.88) at KJ.

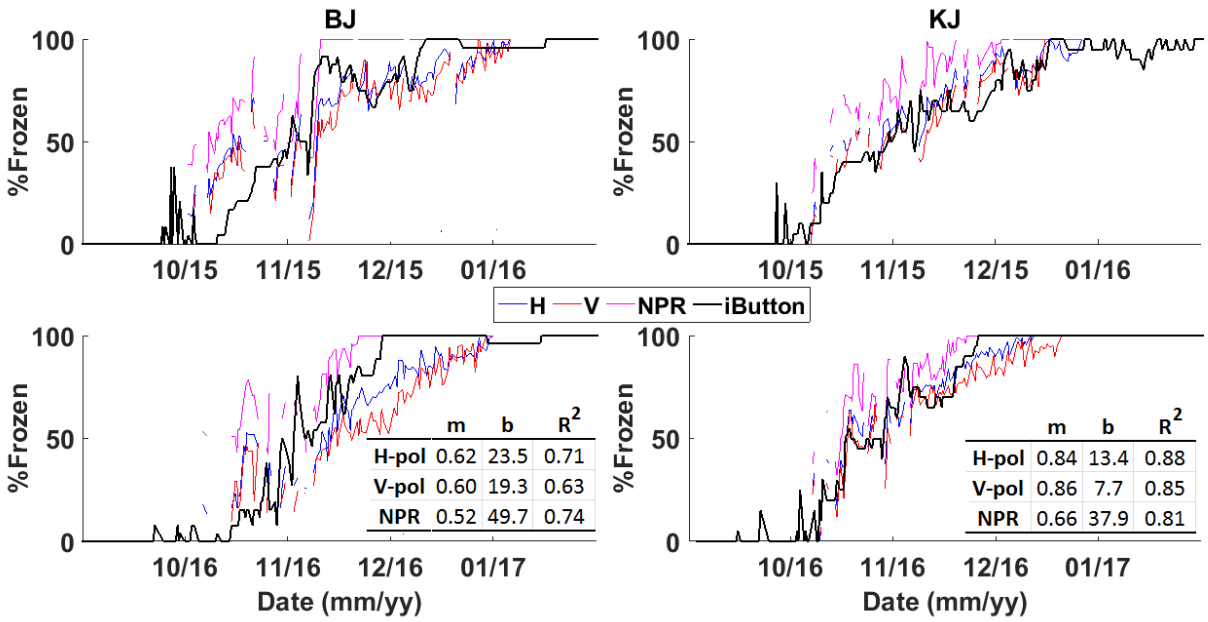

Figure 4 : : Time series for 2015-2016 (top) and 2016-2017 (bottom) of the percentage frozen soil estimated by SMAP (%frox) using the H, V and NPR observations compared to the percentage frozen soil observed by the iButtons (Ffro). BJ at left and KJ at right. The table in the lower right shows the regression line slope (m) and intercept (b) and R2 of the scatter graphs between Ffro and %frox calculated by combining the two years for each site.

However, there are some observable differences between F_{fro} and the $\%fro_x$ estimates. First, F_{fro} detects an early non-permanent freeze at both sites, while the SMAP algorithm does not. In addition, $\%fro_H$, $\%fro_V$ and $\%fro_{NPR}$ often start with high values of $\%fro_x$ early in the freezing process before catching up to the F_{fro} curve. Lastly, $\%fro_{NPR}$ always detects 100% frozen soil earlier (16 days on average) than the iButtons, while $\%fro_H$ and $\%fro_V$ reach 100% frozen later (24 days on average). This $\%fro_x$ behavior is discussed in Section 4.

4. Discussion

Successfully estimating F_{fro} using the iButtons and simulating TBs approaching SMAP TBs required an approach with two temperature thresholds (T1 and T2) to consider the coexistence of the frozen and thawed states during transition periods and within a SMAP pixel area (~ 40 km). Using soil FT radiometry (Rautiainen et al., 2014) shows that when soil temperature reaches its point of fusion, the thermal transfer of latent heat begins. During this process, even if the temperature remains constant, the TB and NPR signals vary in reaction to the phase change. This physical process must therefore be represented in the ω-τ model. Other potential techniques may have been developed, but we considered that the simple two-threshold technique adequately described the phase change process. T1 and T2 were optimized solely with one year (2016) of AM data from a single site (BJ). Since the results are reproducible when PM data, another year (BJ, 2017) and another site (KJ, 2016 and 2017) are included, the inversion is applicable. It should be noted that the T2 = 0.3°C threshold incorporates the measured iButton bias to represent the freezing point of water at 0°C.

Even though the number of iButtons is limited and their distribution does not cover an entire pixel (Fig. 1), the estimation of the spatial variability of soil FT with F_{fro} within the SMAP pixel is an approximation. Nonetheless, the T_{soil} measurements showed significant variability in frozen soil that agree with the SMAP observations. We believe it is a first step for a better understanding of SMAP signal, which will require further investigation.

In that sense, some of the error from our frozen fraction algorithm may be due to the fact that the iButtons do not perfectly represent all intra-pixel soil temperatures. Rowlandson et al. (2018) showed that the NPR and L-band soil freezing estimation algorithms represent the first centimeter of frozen soil. Hence, the large variations in SMAP TB and NPR data during freeze and thaw periods are not connected to a soil freeze depth effect, but rather to a frozen soil intra-pixel surface effect. Furthermore, the findings pointed to only a weak correlation between the moment of freezing and vegetation density, while soil types were not able to explain soil freezing timing. Vegetation can have a significant impact on the spatial variability of snow (Busseau et al., 2017). Consequently, we believe that the snow insulating effect is the main cause of soil freezing variability in fall (Domine et al., 2015).

Since the ω-τ model is semi-empirical, using it for calculations requires that certain parameters be determined by inversion from real measurements. The techniques described in Sections 2.4.2 and 2.4.3 were carefully chosen to obtain Γ_H, Γ_V, and γ values corresponding to the values found in the literature. The values obtained in this study are on the same order as those in other studies, with winter values of $\gamma\_{BJ} = 0.87$ and $\gamma\_{KJ} = 0.88$, which are similar to [0.83-0.84] (Mavrovic et al., 2018) and [0.87-0.88] (Zheng et al., 2017). For summer, $\gamma\_{BJ} \approx 0.62$ and $\gamma\_{KJ} = 0.78$ are comparable to [0.57-0.60] (Zheng, 2017), [0.62-0.69] (Mavrovic et al., 2018) and [0.43-0.75] (Grant et al., 2008). Despite some underlying assumptions on the use of the ω-τ model, this method made it possible to show the effect of spatial variability in soil freezing on the SMAP signal.

This study also disregarded the snow effect. Dry snow can have some impact on TB in L-band, particularly at larger angles (Lemmetyinen et al., 2016). However, that effect is much less significant than soil FT, particularly for radiometers with an incidence angle of 40°, such as SMAP (Roy et al., 2017a). Furthermore, SMAP observations are highly influenced by thawing episodes and wet snow. While this study identified these variations using weather station air temperature readings, developing a more robust wet snow detection algorithm could help simplify the implementation of an operational freeze fraction product (Schwank et al., 2018; Pellarin et al., 2016).

Lastly, the $\%fro_x$ estimation algorithm has the advantage to require only SMAP TB data and a T_{air} indicator to determine the beginning of the frozen period. In this study, T_{air} came from weathers stations. For a global application, it would be possible to acquire T_{air} data from weather model reanalysis such as ERA-Interim from the European Centre for Medium-Range Weather Forecasts (ECMWF). This method is already in use in the SMOS (Kerr et al., 2012) and SMAP (Derksen et al., 2017) algorithms. The algorithm developed in this study remains simple and might be limited in large-scale operational applications. The impact of water bodies is also a factor to study, considering their strong influence on the L-band signal (Roy et la., 2015). However, the goal of this study was to demonstrate the potential of L-band satellite measurements in frozen soil detection in boreal forest. Other studies will be required to make the algorithm operational at a large scale.

5. Conclusion

This study showed that the spatial variability of fall soil freezing on two sites in northern boreal forest is observable and that it has a significant impact on SMAP L-band brightness temperature radiometer measurements during fall transition periods. Using field measurements spatially distributed in a pixel, it showed that this progressive freeze period can extend to up to 9.5 weeks. Disregarding this variability could significantly bias studies on the impact of soil freezing in the fields of biogeosciences (carbon flux, photosynthesis, etc.), hydrology (erosion) and permafrost. Based on these observations, the study proposes a new algorithm for frozen soil fraction in boreal forest using SMAP and T_{air} observations. This algorithm offers an improvement over the one currently used by SMAP and makes it possible to extract more information from satellite radiometer measurements. On a global scale, the algorithm would allow more detailed and accurate monitoring of soil freezing in boreal forest during the crucial transition periods. This in turn would make it possible to better quantify the potential effect of the differential evolution of frozen soil on various biogeophysical processes such as boreal forest carbon flux.

Ackowledgements

This work was made possible thanks to the contributions of the Canadian Space Agency (CSA), Natural Sciences and Engineering Research Council of Canada (NSERC), Canada Foundation

for Innovation (CFI), Center for Northern Studies (CEN), Northern Scientific Training Program (NSTP) and the “Fond de Recherche Nature et Technologiques” (FRQNT). We like to thank the NSIDC (National Snow and Ice Data Center) for the SMAP data distribution. Finally, the realization of fieldworks for this study was made with the help of our colleagues Patrick Cliche, Nicolas Marchand, Bruno-Charles Busseau, Gabriel Diab and Alex Mavrovic.

References

Barr, A., Black, T. A., & Mccaughey, H. (2009). *Phenology of Ecosystem Processes*. (P. of E. Processes, Ed.) (A. Noormet). https://doi.org/10.1007/978-1-4419-0026-5

Black, T. A., Nesic, Z., Chen, Z., Chen, W. J., Barr, A. G., Arain, M. A., et al. (2000). Increased carbon sequestration by a boreal deciduous forest in years with a warm spring. *Geophysical Research Letters*, *27*(9), 1271–1274.

Brodzik, M. J., & Knowles, K. (2011). EASE-Grid 2.0 Land Cover Classifications Derived from Boston University MODIS/Terra Land Cover Data, Version 1. https://doi.org/http://dx.doi.org/10.5067/XR8523MC24TB

Commission canadienne de pedologie (1987) Le systeme canadien de classification des sols. *Publication 1646 du Ministere de l'Agriculture du Canada*, Approvisionnements et Services Canada, Ottawa, 170 p.

Chan, S. K., Member, S., Bindlish, R., Neill, P. E. O., Njoku, E., Jackson, T., et al. (2016). Assessment of the SMAP Passive Soil Moisture Product, 1–14.

Chan, S., Bindlish, R., Hunt, R., Jackson, T., & Kimball, J. (2013). Ancillary Data Report: Landcover Classification. *Jet Propulsion Laboratory California Institute of Technology*, (SMAP Science Document no. 042).

Derksen, C., Xu, X., Scott Dunbar, R., Colliander, A., Kim, Y., Kimball, J. S., et al. (2017). Retrieving landscape freeze/thaw state from Soil Moisture Active Passive (SMAP) radar and radiometer measurements. *Remote Sensing of Environment*, *194*, 48–62. https://doi.org/10.1016/j.rse.2017.03.007

Didan, K., (2015), MODIS/Aqua Vegetation Indices 16-Day L3 Global 1km V006. NASA EOSDIS Land Processes DAAC, *USGS Earth Resources Observation and Science* (EROS) Center, Sioux Falls, South Dakota (https://lpdaac.usgs.gov), accessed [10-16-2017], at http:// dx.doi.org 10.5067/MODIS/MYD13A2.006

Domine, F., Barrere, M., Sarrazin, D., Morin, S., & Arnaud, L. (2015). Automatic monitoring of the effective thermal conductivity of snow in a low-Arctic shrub tundra. *Cryosphere*, *9*(3), 1265–1276. https://doi.org/10.5194/tc-9-1265-2015

Gouttevin, I., Menegoz, M., Dominé, F., Krinner, G., Koven, C., Ciais, P., et al. (2012). How the insulating properties of snow affect soil carbon distribution in the continental pan-Arctic area. *Journal of Geophysical Research: Biogeosciences*, *117*(2), 1–11. https://doi.org/10.1029/2011JG001916

Gray, D.M.; Landine, P.G.; Granger, R. J. (1984). Simulating infiltration into frozen Prairie soils in streamflow models. *Canadian Journal Earth Science*, *22*, 464–472.

Huete, A., & Justice, C. (1999). Modis Vegetation Index Algorithm Theoretical Basis. *Environmental Sciences*, (Mod 13), 129. https://doi.org/10.1016/j.rse.2007.07.019

Kerr, Y. H., Waldteufel, P., Richaume, P., Wigneron, J. P., Ferrazzoli, P., Mahmoodi, A., et al. (2012). The SMOS Soil Moisture Retrieval Algorithm. *Geoscience and Remote Sensing*, *50*(5), 1384–1403. https://doi.org/10.1109/TGRS.2012.2184548

Kim, Y., Kimball, J. S., Zhang, K., & McDonald, K. C. (2012). Satellite detection of increasing Northern Hemisphere non-frozen seasons from 1979 to 2008: Implications for regional vegetation growth. *Remote Sensing of Environment*, *121*, 472–487. https://doi.org/10.1016/j.rse.2012.02.014

Kim, Y., Kimball, J. S., McDonald, K. C., & Glassy, J. (2011). Developing a global data record of daily landscape freeze/thaw status using satellite passive microwave remote sensing. *IEEE Transactions on Geoscience and Remote Sensing*, *49*(3), 949–960. https://doi.org/10.1109/TGRS.2010.2070515

Kumar, N., Grogan, P., Chu, H., Christiansen, C. T., Walker, V. K., & Sciences, M. (2013). The Effect of Freeze-Thaw Conditions on Arctic Soil Bacterial Communities. *Biology*, *2*, 356–377. https://doi.org/10.3390/biology2010356

Kurganova, I., Teepe, R., & Loftfield, N. (2007). Influence of freeze-thaw events on carbon dioxide emission from soils at different moisture and land use. *Carbon Balance and Management*, *9*, 1–9. https://doi.org/10.1186/1750-0680-2-2

Lemmetyinen, J., Schwank, M., Rautiainen, K., Kontu, A., Parkkinen, T., Mätzler, C., et al. (2016). Snow density and ground permittivity retrieved from L-band radiometry: Application to experimental data. *Remote Sensing of Environment*, *180*, 377–391. https://doi.org/10.1016/j.rse.2016.02.002

Lundquist, J. D., & Lott, F. (2008). Using inexpensive temperature sensors to monitor the duration and heterogeneity of snow-covered areas. *Water Resource Research*, *44*, 8–13. https://doi.org/10.1029/2008WR007035

Mahecha, D., Reichstein, M., Carvalhais, N., Lasslop, G., Lange, H., Seneviratne, S., et al. (2010). References and Notes 1., *329*(August), 838–841.

Massari, C., Brocca, L., Pellarin, T., Kerr, Y., Crow, W., Cascon, C., & Ciabatta, L. (2016). Rainfall estimation over-land using SMOS soil moisture observations: SM2RAIN, LMAA and SMART algorithms. *EGU General Assembly Conference Abstracts*, *18*, 8521.

Mavrovic, A., Roy, A., Royer, A., Filali, B., Boone, F., Pappas, C., & Sonnentag, O. (2018). Dielectric characterization of vegetation at L band using an open-ended coaxial probe. *Geoscientific Instrumentation, Methods and Data Systems*, *7*(3), 195–208. https://doi.org/10.5194/gi-7-195-2018

McGuire, A. D., Christensen, T. R., Hayes, D., Heroult, A., Euskirchen, E., Kimball, J. S., et al. (2012). An assessment of the carbon balance of Arctic tundra: Comparisons among observations, process models, and atmospheric inversions. *Biogeosciences*, *9*(8), 3185–3204. https://doi.org/10.5194/bg-9-3185-2012

Meriaux, S. (1954). Contribution à l'étude de l'analyse granulométrique. *Annales agronomiques (Dijon, France)*, Serie A, vol. 5, n° 1, p. 5-59 et n° 2, p. 149-205

Mo, T., Choudhury, B. J., Schmugge, T. J., Wang, J. R., & Jackson, T. J. (1982). A model for microwave emission from vegetation-covered fields. *Journal of Geophysical Research*, *87*(1), 11229–11237. https://doi.org/10.1029/JC087iC13p11229

O'Neill, P., Chan, S., Njoku, E., Jackson, T., & Bindlish, R. (2015). Soil Moisture Active Passive (SMAP) Algorithm Theoretical Basis Document Level 2 & 3 Soil Moisture (Passive) Data Products. *Jet Propulsion Laboratory California Institute of Technology*.

Pachauri, R. K. (2014). *Climate Change 2014 Synthesis Report*.

Peng, X., Frauenfeld, O. W., Cao, B., Wang, K., Wang, H., Su, H., et al. (2016). Response of changes in seasonal soil freeze/thaw state to climate change from 1950 to 2010 across china. *Journal of Geophysical Research: Earth Surface*, (121), 1984–2000. https://doi.org/10.1002/2016JF003876

Poutou, E., Krinner, G., & Genthon, C. (2004). Role of soil freezing in future boreal climate change. *Climate Dynamics*, (23), 621–639. https://doi.org/10.1007/s00382-004-0459-0

Prince, M., Roy, A., Brucker, L., Royer, A., Kim, Y., & Tianjie, Z. (Under review). Northern Hemisphere Surface Freeze/Thaw Product from Aquarius L-band Radiometers. *Earth System Science Data*, (March), 1–29. https://doi.org/10.5194/essd-2018-25

Rautiainen, K., Lemmetyinen, J., Pulliainen, J., Vehvilainen, J., Drusch, M., Kontu, A., et al. (2012). L-band radiometer observations of soil processes in boreal and subarctic environments. *IEEE Transactions on Geoscience and Remote Sensing*, *50*(5 PART 1), 1483–1497. https://doi.org/10.1109/TGRS.2011.2167755

Rautiainen, K., Lemmetyinen, J., Schwank, M., Kontu, A., Ménard, C. B., Mätzler, C., et al. (2014). Detection of soil freezing from L-band passive microwave observations. *Remote Sensing of Environment*, *147*, 206–218. https://doi.org/10.1016/j.rse.2014.03.007

Rautiainen, K., Parkkinen, T., Lemmetyinen, J., Schwank, M., Wiesmann, A., Ikonen, J., et al. (2016). SMOS prototype algorithm for detecting autumn soil freezing. *Remote Sensing of Environment*, *180*, 346–360. https://doi.org/10.1016/j.rse.2016.01.012

Rowlandson, T. L., Berg, A. A., Roy, A., Kim, E., Pardo, R., Powers, J., et al. (2018). Capturing agricultural soil freeze / thaw state through remote sensing and ground observations : A soil freeze / thaw validation campaign. *Remote Sensing of Environment*, *211*(April), 59–70. https://doi.org/10.1016/j.rse.2018.04.003

Roy, A., Royer, A., Derksen, C., Brucker, L., Langlois, A., Mialon, A., & Kerr, Y. H. (2015). Evaluation of Spaceborne L-Band Radiometer Measurements for Terrestrial Freeze/Thaw Retrievals in Canada. *IEEE Journal of Selected Topics in Applied Earth Observations and Remote Sensing*, *8*(9), 4442–4459. https://doi.org/10.1109/JSTARS.2015.2476358

Roy, A., Toose, P., Derksen, C., Rowlandson, T., Berg, A., Lemmetyinen, J., et al. (2017a). Spatial Variability of L-Band Brightness Temperature during Freeze / Thaw Events over a Prairie Environment. *Remote Sensing*, *9*(894), 1–16. https://doi.org/10.3390/rs9090894

Roy, A., Toose, P., Williamson, M., Rowlandson, T., Derksen, C., Royer, A., et al. (2017b). *Response of L-Band brightness temperatures to freeze/thaw and snow dynamics in a prairie environment from ground-based radiometer measurements*. *Remote Sensing of Environment* (Vol. 191). Elsevier Inc. https://doi.org/10.1016/j.rse.2017.01.017

Schaeffer, Kevin; Zhang, Tingjun, Bruhwiler, Lori; Barrett, A. P. (2011). Amount and timing of permafrost carbon release in response to climate warming. *Tellus*, *63B*, 165–180. https://doi.org/10.1111/j.1600-0889.2011.00527.x

Schuur, E. A. G., McGuire, A. D., Schädel, C., Grosse, G., Harden, J. W., Hayes, D. J., et al. (2015). Climate change and the permafrost carbon feedback. *Nature*, *520*(7546), 171–179. https://doi.org/10.1038/nature14338

Schwank, M., & Naderpour, R. (2018). Snow density and ground permittivity retrieved from L-band radiometry: Melting effects. *Remote Sensing*, *10*(2), 1–26. https://doi.org/10.3390/rs10020354

Schwank, M., Stähli, M., Wydler, H., Leuenberger, J., Mätzler, C., Member, S., & Flühler, H. (2004). Microwave L-Band Emission of Freezing Soil. *IEEE Transactions on Geoscience and Remote Sensing*, *42*(6), 1252–1261.

Selvam, B. P., Laudon, H., Guillemette, F., & Berggren, M. (2016). Influence of soil frost on the character and degradability of dissolved organic carbon in boreal forest soils. *Journal of Geophysical Research: Biogeosciences RESEARCH*, 829–840. https://doi.org/10.1002/2015JG003228.Received

Strahler, A., Gopal, S., Lambin, E., & Moody, A. (1999). MODIS Land Cover Product, Algorithm Theoretical Basis Document (ATBD). *Change*, (May 1999), 72. Retrieved from http://modis.gsfc.nasa.gov/data/atbd/atbd_mod12.pdf

Suni, T., Rinne, J., Reissell, A., Altimir, N., Keronen, P., Rannik, U., et al. (2003). Long-term measurements of surface fluxes above a Scots pine forest in Hyytiala, southern Finland, 1996-2001. *Boreal Environment Research*, *8*(4), 287–301. Retrieved from http://research.eeescience.utoledo.edu/lees/papers_PDF/Suni_2003_BorEnvRes.pdf%5Cn%3CGo to ISI%3E://WOS:000221372700003

Ter-Mikaelian, M. T., & Korzukhin, M. D. (1997). Biomass equations for sixty-five North American tree species. *Forest Ecology and Management*, *97*(1), 1–24. https://doi.org/10.1016/S0378-1127(97)00019-4

Wigneron, J. P., Kerr, Y., Waldteufel, P., Saleh, K., Escorihuela, M. J., Richaume, P., et al. (2007). L-band Microwave Emission of the Biosphere (L-MEB) Model: Description and calibration against experimental data sets over crop fields. *Remote Sensing of Environment*, *107*(4), 639–655. https://doi.org/10.1016/j.rse.2006.10.014

Wigneron, J., Jackson, T. J., Neill, P. O., Lannoy, G. De, Rosnay, P. De, Walker, J. P., et al. (2017). Modelling the passive microwave signature from land surfaces : A review of recent results and application to the L-band SMOS & SMAP soil moisture retrieval algorithms. *Remote Sensing of Environment*, *192*(January), 238–262. https://doi.org/10.1016/j.rse.2017.01.024

Xu, L., Myneni, R. B., Iii, F. S. C., Callaghan, T. V, Pinzon, J. E., Tucker, C. J., et al. (2013). Temperature and vegetation seasonality diminishment over northern lands. *Nature Climate Change*, (March), 1–6. https://doi.org/10.1038/nclimate1836

Zheng, D., Wang, X., Velde, R. Van Der, Zeng, Y., Wen, J., Wang, Z., et al. (2017). L-Band Microwave Emission of Soil Freeze – Thaw Process in the Third Pole Environment. *IEEE Transactions on Geoscience and Remote Sensing*, *55*(9), 5324–5338.

4. Conclusion générale

Ce mémoire de maîtrise est d'abord une étude à l'échelle de l'Hémisphère Nord (> 50°N), puis sur une étude locale en forêt boréale sur la télédétection micro-ondes passives des cycles de gel/dégel. D'abord, ce travail a aidé à la publication d'un nouveau produit de gel/dégel en bande L issu des radiomètres d'Aquarius disponible sur le site du NSIDC en évaluant spatialement et temporellement le comportement du produit. Ensuite, il a abouti à la conception d'un nouvel algorithme d'estimation du gel/dégel permettant de quantifier le pourcentage de sol gelé à l'intérieur d'un pixel à l'aide des observations du satellite SMAP.

Le premier projet de cette maîtrise a évalué avec succès un nouveau produit de gel/dégel en bande L. La publication du nouveau produit de gel/dégel d'Aquarius assure, avec la mission SMAP actuellement opérationnelle, un continuum d'observations de micro-ondes passives en bande L faites par les radiomètres satellitaires de la NASA, pour une période commençant en août 2011. Le travail a effectué une intercomparaison entre deux produits de gel/dégel à différentes fréquences (1.4 GHz et 37 GHz). Les résultats montrent qu'il existe des différences assez fortes en toundra, plutôt faibles en forêt et des comportements variables dans les régions à milieux ouverts. Ces différences, plus ou moins prononcées, peuvent provenir de différences algorithmiques dans la conceptualisation des produits, mais également, des propriétés distinctes des fréquences de radiations micro-ondes.

Le deuxième projet a réussi à observer la variabilité spatiale du gel/dégel en forêt boréale. Grâce à une modélisation de l'émission des micro-ondes de l'environnement à partir de mesures in situ et de paramètres ajustés, il a été possible de simuler le comportement des mesures de TB de SMAP durant les périodes automnales de transition du gel/dégel. En montrant ainsi que SMAP est sensible au gel/dégel du sol, l'algorithme utilisé par l'équipe de SMAP a été amélioré pour passer d'une mesure qualitative binaire à une mesure quantitative de pourcentage intrapixel de sol gelé. Une prochaine étape pour l'utilisation de cet algorithme serait d'évaluer son application à grande échelle. La difficulté de cette tâche est que la validation de l'algorithme nécessite des réseaux intrapixel de mesures de températures du sol, ce qui est très rare en forêt boréale. Une étude pourrait être faite avec les sites de validation de l'équipe de SMAP ou de SMOS, mais ceux-ci sont présentement concentrés dans des zones agricoles. Toutefois, l'équipe de SMAP

planifie une campagne (SMAPVEX21) de calibration et de validation de ses produits en forêt boréale en 2021, ce qui sera une bonne opportunité de développer des transects intrapixel de mesures de températures du sol. Il serait également intéressant d'étudier le lien entre les transitions de gel/dégel et le flux de CO_2. Les valeurs estimées par l'algorithme de % de gel pourrait être mises en relation avec des séries temporelles de production primaire brute et d'échange écosystémique net de CO_2 provenant d'analyses de tours de covariance des turbulences (flux de CO_2). Les nouvelles données de gel/dégel pourraient aussi être insérées dans les modèles écosystémiques de calcul du bilan de CO_2 pour voir l'impact sur les bilans de carbone modélisés.

À notre connaissance, il n'existe pas d'étude portant sur l'analyse de la variabilité spatiale de la température du sol et du pourcentage de surface gelée dans un pixel micro-onde en milieu boréal. La base de données qu'offrent les deux années de mesures iButton sur deux sites, BJ et KJ, est ainsi une source d'information privilégiée. Cette série possède encore un riche potentiel d'information à exploiter. Entre autres, chaque emplacement de iButton contient également une mesure à 5 cm de profondeur dans le sol. Ainsi, il serait intéressant d'étudier s'il y a un effet de profondeur de gel relié à la mesure de SMAP. De plus, une troisième année de données de iButton va prochainement s'ajouter à la série, permettant de vérifier la reproductibilité de la technique utilisée dans cette étude. Une analyse interannuelle pourrait se faire sur les différents comportements du gel/dégel de l'environnement (saisons chaudes ou froides, nombres de redoux, épisodes de pluie sur neige, etc.) afin de les relier aux réactions des signaux de SMAP.

Une prochaine étape logique à ces deux projets serait d'utiliser la base de données des iButton et d'analyser en parallèle les TB à multiples fréquences, en prenant les données de la mission AMSR-2 (*Advanced Microwave Scanning Radiometer*) à 6.93 GHz, 7.3 GHz, 10.65 GHz, 18.7 GHz, 23.8 GHz et 36.5 GHz, pour éventuellement créer un produit gel/dégel amélioré multifréquences. Ce travail conclut qu'une comparaison au niveau des TB des diverses fréquences pourrait aider à comprendre la raison des divergences entre les produits et permettre de mettre à profit l'information issue de différentes fréquences micro-ondes. Pour conclure, le travail réalisé par ce projet de maîtrise offrira à la communauté scientifique des outils pour mieux comprendre et quantifier les cycles de gel/dégel de l'environnement boréal et éventuellement, pour mieux quantifier les flux de carbone, les crues printanières et l'évolution du pergélisol.

5. Références hors articles

Artemov, V.G., et Volkov A.A. (2014). Water and Ice Dielectric Spectra Scaling at 0°C. *Ferroelectrics*, vol. 466, no° 1, p. 158–165.

Barr, A., Black T.A., McCaughey H. (2009) Climatic and Phenological Controls of the Carbon and Energy Balances of Three Contrasting Boreal Forest Ecosystems in Western Canada. In: Noormets A. (eds), *Phenology of Ecosystem Processes*. Springer, New York, NY

Beer, C, W Lucht, D Gerten, K Thonicke, and C Schmullius. (2007). Effects of Soil Freezing and Thawing on Vegetation Carbon Density in Siberia: A Modeling Analysis with the Lund-Potsdam-Jena Dynamic Global Vegetation Model (LPJ-DGVM). *Global Biogeochemical Cycles*, vol. 21, no° 1, p. 1–14.

Brucker, L, EP Dinnat, and LS Koenig. (2014). Weekly Gridded Aquarius L-Band Radiometer/Scatterometer Observations and Salinity Retrievals over the Polar Regions - Part 1: Product Description. *Cryosphere*, vol. 8, no° 3, p. 905–913.

Demontoux, F, B Le Crom, G Ruffié, JP Wigneron, J. Grant, VL Mironov, and H Lawrence. (2004). High Density Plasma Enhanced Chemical Vapor Deposition of Optical Thin Films. *The European Physical Journal Applied Physics*, vol. 28, no° December, p. 265–291.

Derksen, C, X Xu, R Scott Dunbar, A Colliander, Y Kim, JS Kimball, TA Black, et al. (2017). Retrieving Landscape Freeze/Thaw State from Soil Moisture Active Passive (SMAP) Radar and Radiometer Measurements. *Remote Sensing of Environment*, vol. 194, Elsevier Inc., p. 48–62.

Derksen, C, AE Walker, BE Goodison, and JW Strapp. (2005). Integrating In Situ and Multiscale Passive Microwave Data for Estimation of Subgrid Scale Snow Water Equivalent Distribution and Variability, *IEEE Transactions on geoscience and remote sensing,* vol. 43, no° 5, p. 960–972.

Derksen, Chris, Anne E Walker, Barry E Goodison, and J Walter Strapp. 2005. “Integrating In Situ and Multiscale Passive Microwave Data for Estimation of Subgrid Scale Snow Water Equivalent Distribution and Variability.” *IEEE* 43 (5): 960–72.

Entekhabi, D, EG Njoku, PE O’Neill, KH Kellogg, WT Crow, WN Edelstein, JK Entin, et al. (2010). The Soil Moisture Active Passive (SMAP) Mission. *Proceedings of the IEEE*, vol. 98, no° 5, p. 704–716.

FAO Production yearbook (1999). Food and Agriculture Organization of the United Nations, vol 53. Stastical series no. 156 2001FAO; Rome, Italy.

Gauthier, S, P Bernier, T Kuuluvainen, AZ Shvidenko, and DG Schepaschenko. (2015). Forest Health and Global Change. *Science*, vol. 349, no° 6250, p. 814–18.

Goulden, ML. (1998). Sensitivity of Boreal Forest Carbon Balance to Soil Thaw. *Science*, vol. 279, no° 5348, p. 214–217.

Gouttevin, I, M Menegoz, F Dominé, G Krinner, C Koven, P Ciais, C Tarnocai, and J Boike. (2012). How the Insulating Properties of Snow Affect Soil Carbon Distribution in the Continental Pan-Arctic Area. *Journal of Geophysical Research: Biogeosciences*, vol. 117, no° 2, p. 1–11.

Kerr, Y, Waldteufel Philippe, Wigneron Jean-Pierre, Delwart S., Cabot François, et al. (2010). The SMOS mission: new tool for monitoring key elements of the global water cycle. *Proceedings of the IEEE*, vol. 98, no.5, p.666-687.

Kerr, Y., 1996. Optimal choice for miras frequencies scientific requirements. CESBIO, Report

Kim, Y, JS Kimball, K Zhang, K Didan, and I Velicogna. (2014). Attribution of Divergent Northern Vegetation Growth Responses to Lengthening Non-Frozen Seasons Using Satellite Optical-NIR and Microwave Remote Sensing. *International Journal of Remote Sensing*, vol. 35, no° 10, Taylor & Francis p. 3700–3721.

Kim, Y, JS Kimball, K Zhang, and KC McDonald. (2012). Satellite Detection of Increasing Northern Hemisphere Non-Frozen Seasons from 1979 to 2008: Implications for Regional Vegetation Growth. *Remote Sensing of Environment*, vol. 121, Elsevier Inc., p. 472–487.

Kim, Y, JS Kimball, KC McDonald, and J Glassy. (2011). Developing a Global Data Record of Daily Landscape Freeze/Thaw Status Using Satellite Passive Microwave Remote Sensing. *IEEE Transactions on Geoscience and Remote Sensing*, vol. 49, no° 3, p. 949–960.

Kim, Y, JS Kimball, J Glassy, and J Du. (2017). An Extended Global Earth System Data Record on Daily Landscape Freeze – Thaw Status Determined from Satellite Passive Microwave Remote Sensing. *Earch System Science Data*, p.133–147.

Langlois, A, A Royer, F Dupont, A Roy, K Goita, and G Picard. (2011). Improved Corrections of Forest Effects on Passive Microwave Satellite Remote Sensing of Snow over Boreal and Subarctic Regions. *IEEE Transactions on Geoscience and Remote Sensing*, vol. 49, no° 10 PART 2, p. 3824–3837.

Vine, DM Le, GSE Lagerloef, and SE Torrusio. (2010). Aquarius and Remote Sensing of Sea Surface Salinity from Space. *Proceedings of the IEEE*, vol. 98, no° 5, p. 688–703.

Lemmetyinen, J, M Schwank, K Rautiainen, A Kontu, T Parkkinen, C Mätzler, A Wiesmann, et al. (2016). Snow Density and Ground Permittivity Retrieved from L-Band Radiometry:

Application to Experimental Data. *Remote Sensing of Environment*, vol. 180, Elsevier Inc., p. 377–391.

Mironov, VL, K V. Muzalevskiy, and I V. Savin. (2013). Retrieving Temperature Gradient in Frozen Active Layer of Arctic Tundra Soils from Radiothermal Observations in L-Band-Theoretical Modeling. *IEEE Journal of Selected Topics in Applied Earth Observations and Remote Sensing*, vol. 6, no° 3, p. 1781–1785.

Nalder, I.A., and RW Wein. (1998). Spatial Interpolation of Climatic Normals: Test of a New Method in the Canadian Boreal Forest. *Agricultural and Forest Meteorology*, vol. 92, p. 211–225.

New, M, M Hulme, and P Jones. (2000). Representing Twentieth-Century Space-Time Climate Variability. Part II: Development of 1901-96 Monthly Grids of Terrestrial Surface Climate. *Journal of Climate*, vol. 13, no° 13, p. 2217–2238.

Parazoo, NC, A Arneth, TAM Pugh, B Smith, N Steiner, K Luus, R Commane, et al. (2018). Spring Photosynthetic Onset and Net CO2uptake in Alaska Triggered by Landscape Thawing. *Global Change Biology*, no. March p. 3416–3435.

Picard, G, L Brucker, A Roy, F Dupont, M Fily, A Royer, and C Harlow. (2013). Simulation of the Microwave Emission of Multi-Layered Snowpacks Using the Dense Media Radiative Transfer Theory: The DMRT-ML Model. *Geoscientific Model Development*, vol. 6, no° 4, p. 1061–1078.

Rautiainen, K, J Lemmetyinen, J Pulliainen, J Vehvilainen, M Drusch, A Kontu, J Kainulainen, and J Seppänen. (2012). L-Band Radiometer Observations of Soil Processes in Boreal and Subarctic Environments. *IEEE Transactions on Geoscience and Remote Sensing*, vol. 50, no° 5 PART 1, p. 1483–1497.

Rautiainen, K, J Lemmetyinen, M Schwank, A Kontu, CB Ménard, C Mätzler, M Drusch, A Wiesmann, J Ikonen, and J Pulliainen. (2014). Detection of Soil Freezing from L-Band Passive Microwave Observations. *Remote Sensing of Environment*, vol. 147, Elsevier Inc., p. 206–218.

Rautiainen, K, T Parkkinen, J Lemmetyinen, M Schwank, A Wiesmann, J Ikonen, C Derksen, et al. (2016). SMOS Prototype Algorithm for Detecting Autumn Soil Freezing. *Remote Sensing of Environment*, vol. 180, p. 346–360.

Rowlandson, TL, AA Berg, A Roy, E Kim, R Pardo, J Powers, K Lewis, et al. (2018). Capturing Agricultural Soil Freeze / Thaw State through Remote Sensing and Ground Observations : A Soil Freeze / Thaw Validation Campaign. *Remote Sensing of Environment*, vol. 211, p. 59–70.

Roy, A., L. Brucker, M. Prince, A. Royer, and C. Derksen. (2018). Aquarius L3 Weekly Polar-Gridded Landscape Freeze/Thaw Data, Version 5. Boulder, Colorado USA. NSIDC: National Snow and Ice Data Center. doi: https://doi.org/10.5067/OV4R18NL3BQR.

Roy, A, P. Toose, C Derksen, T Rowlandson, A Berg, J Lemmetyinen, A Royer, E Tetlock, W Helgason, and O Sonnentag. (2017a). Spatial Variability of L-Band Brightness Temperature during Freeze / Thaw Events over a Prairie Environment. *Remote Sensing*, vol. 9, no° 894, p. 1–16.

Roy, A, P. Toose, M. Williamson, T. Rowlandson, C. Derksen, A. Royer, A.A. Berg, J. Lemmetyinen, and L. Arnold. (2017b). Response of L-Band Brightness Temperatures to Freeze/Thaw and Snow Dynamics in a Prairie Environment from Ground-Based Radiometer Measurements. *Remote Sensing of Environment,* Vol. 191, Elsevier Inc., p.67-80.

Roy, A., A. Royer, O. St-Jean-Rondeau, B. Montpetit, G. Picard, A. Mavrovic, N. Marchand, and A. Langlois. (2015). Microwave Snow Emission Modeling Uncertainties in Boreal and Subarctic Environments. *The Cryosphere, vol.* 9, no. 5, p.5719–5773.

Ruckstuhk, KE, EA Johnson, and K Miyanishi. (2008). Introduction: The Boreal Forest and Global Change. *Philosophical Transaction of the Royal Society*, vol. 363 p. 2245–2249.

Rutter, N, M Sandells, C Derksen, P Toose, A Royer, B Montpetit, A Langlois, J Lemmetyinen, and J Pulliainen. (2014). Snow stratigraphic heterogeneity within ground-based passive microwave radiometer footprints: Implications for emission modeling. *Journal of Geophysical Research: Earth Surface*, vol. 119, no° 3, p. 550–565.

Schuur, EAG, AD McGuire, C Schädel, G Grosse, JW Harden, DJ Hayes, G Hugelius, et al. (2015). Climate Change and the Permafrost Carbon Feedback. *Nature*, vol. 520, no° 7546, p. 171–179.

Schwank, M, C Matzler, A Wiesmann, U Wegmuller, J Pulliainen, J Lemmetyinen, K Rautiainen, C Derksen, P Toose, and M Drusch. (2015). Snow Density and Ground Permittivity Retrieved from L-Band Radiometry: A Synthetic Analysis. *IEEE Journal of Selected Topics in Applied Earth Observations and Remote Sensing*, vol. 8, no° 8, p. 3833–3845.

Schwank, M, K Rautiainen, C Mätzler, M Stähli, J Lemmetyinen, J Pulliainen, J Vehviläinen, et al. (2014). Model for Microwave Emission of a Snow-Covered Ground with Focus on L Band. *Remote Sensing of Environment*, vol. 154, no° 1, p. 180–191.

Selvam, BP, H Laudon, F Guillemette, and M Berggren. (2016). Influence of Soil Frost on the Character and Degradability of Dissolved Organic Carbon in Boreal Forest Soils. *Journal of Geophysical Research: Biogeosciences RESEARCH*, p.829–840.

Ulaby, F. T., Moore, R. K., & Fung, A. K. (1986). Microwave remote sensing: active and passive. Volume III: from theory to applications. Artech House; Remote Sensing Series, 4.